# ABSTRACT


Title of Dissertation: THE CIRCUIT COMPONENTS OF CONTRAST ADAPTATION IN THE ROD BIPOLAR PATHWAY

Gregory E. Perrin
Doctor of Philosophy, 2022

Dissertation Directed by: Professor Joshua H. Singer
Department of Biology

The mammalian retina processes stimuli over a wide range of light intensities. These stimuli can vary substantially over time. The retina must encode these temporally varying light stimuli into the firing rates of retinal ganglion cells, which convey information from the retina to the brain. This process is called contrast adaptation and relies on circuit-level mechanisms called gain controls. My work seeks to determine which physiological mechanisms within the retina shape the process of adaptation within an inner retinal circuit called the rod bipolar pathway.

This work uses Cre-mediated expression of channelrhodopsin-2 to optogenetically stimulate individual components of the rod bipolar pathway: specifically rod bipolar cells and type-6 cone bipolar cells. This allows for the dissection of mechanisms that shape contrast adaptation within the inner retina, without the significant limitations of paired-patch recording. Much of this work also uses Linear-Nonlinear (L-N) cascade modeling, allowing for the use of naturalistic stimuli to study adaptation.

The first part of this dissertation focuses on several findings that suggest prominent roles for synaptic release from rod bipolar cell terminals, as well as the activity of AII amacrine cells in contrast adaptation within the ON component of the rod bipolar pathway (Chapters 1 & 2). The focus will then switch to experiments examining the OFF component of the rod bipolar pathway (Chapter 3). Finally, this dissertation closes with a series of novel methods developed to address technical challenges that occurred during this work (Chapter 4).

# THE CIRCUIT COMPONENTS OF CONTRAST ADAPTATION IN THE ROD BIPOLAR PATHWAY

by

Gregory E. Perrin

Dissertation submitted to the Faculty of the Graduate School of the
University of Maryland, College Park in partial fulfillment
of the requirements for the degree of
Doctor of Philosophy
2022

Advisory Committee:
Professor Joshua H. Singer, Chair
Professor Daniel A. Butts
Professor Catherine E. Carr
Professor Quentin Gaudry
Professor Matthew Roesch
Professor Colenso Speer

# Table of Contents

# List of Tables

# List of Figures

# Chapter 1: Introduction

## 1.1 Mammalian Retinal Architecture

The retina is an incredibly versatile model for examining how biophysical mechanisms shape computation within neural circuits. The retina's primary computational function, converting complex visual stimuli into ganglion cell spiking, is relatively well understood. Its structure and connectivity are readily identifiable, and it is organized into functionally distinct laminae, making the problem of connecting circuit components to their computational functions a tractable one (Dowling, 2012; Demb and Singer, 2015). Further, the retina develops from the neural tube (the same cells that ultimately develop into the spinal cord and brain, Stenkamp, 2015). In short, the retina is the "most accessible" part of the mammalian central nervous system (Dowling, 2012).

Like much of the CNS, the retina is highly parallelized. It breaks visual signals into multiple streams at nearly every level of processing (Asari and Meister, 2012; Dowling, 2012; Kolb, 2005; Murphy and Rieke, 2006; Park et al., 2018). Identical circuits exist in close proximity to one another, allowing for co-processing of the same information simultaneously (for the same loci in visual space, Dunn and Rieke, 2008). Almost every level of retinal processing shows substantial convergence of presynaptic inputs, and divergence of postsynaptic outputs (Asari and Meister, 2012). Ultimately, this parallel architecture allows for a wide range of complex computations, even before signals reach retinal ganglion cells.

The retina is organized into five distinct layers. First, and outer-most is the photoreceptor layer (PL). The PL is occupied by the eponymous photoreceptors, which are subdivided into two classes: rods and cones ('R' & 'C', Figure 1). Conventionally, rods are responsible for dim-light (scotopic) vision, while cones are responsible for bright-light (photopic) vision (an exception to this will be discussed later, Dowling, 2012). Photoreceptors encode responses to stimuli ranging from as sparse as a single photon, all the way up to bright daylight (an over 10-billion-fold range in intensity, Baylor et al, 1979, 1984, 1996; Field et al., 2005; Dunn et al., 2006; Dunn and Rieke, 2006, 2008; Demb and Singer, 2015). The retina's ability to encode such a wide range of stimuli (through a process called adaptation) is perhaps one its most prominent computational functions. The process of adaptation occurs at nearly every level of the retina, using mechanisms called gain controls (Baccus and Meister, 2002).

Determining the circuit components that shape adaptation is the primary focus of this dissertation. The remainder of this chapter focuses on methods for studying adaptation in the retina. Chapter 2 applies these methods to the ON component of the rod bipolar pathway. Chapter 3 then explores the OFF component of the pathway. Finally, Chapter 4 aims to address some of the technical challenges that have arisen in the course of this work.

### 1.1.1 Adaptation in the outer retina

As light level increases, photoreceptors adapt their response to overall stimulus intensity. This provides the retina with an immediate way of avoiding saturation to the highest intensity stimuli. For the most part, response-amplitude curves do not change shape with adaptation. Rather, the stimulus intensity that drives a given response amplitude shifts with adaptation. The

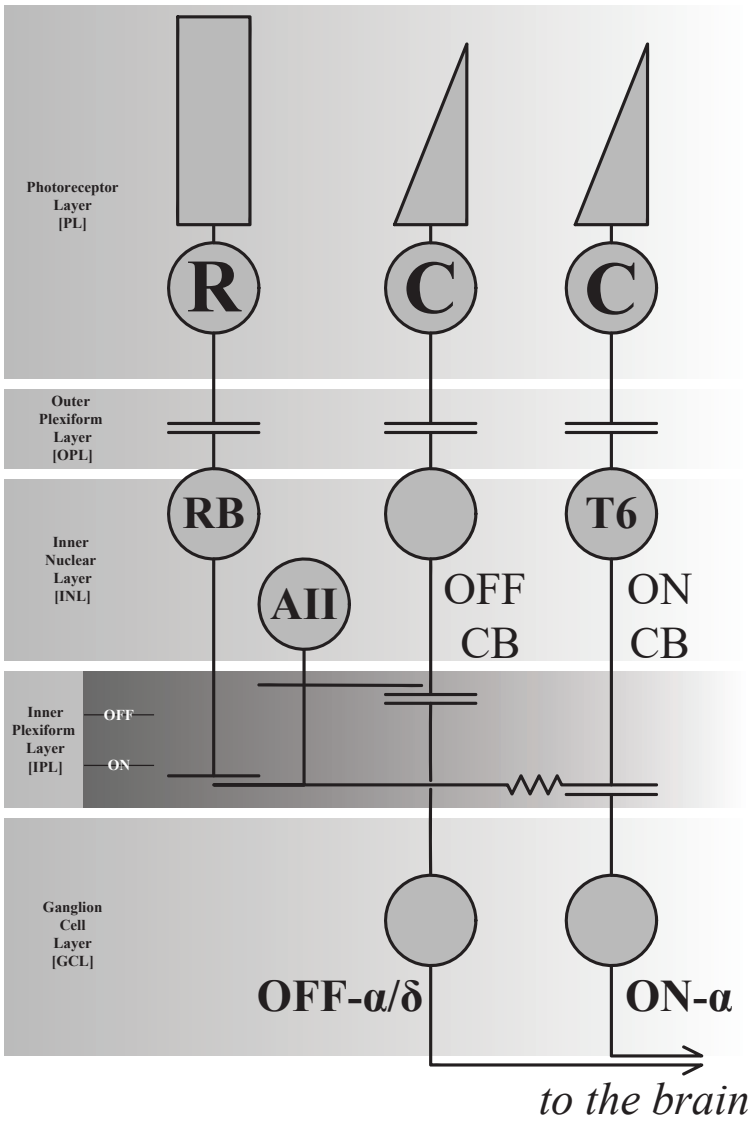


Figure 1.1: Schematic of the rod bipolar pathway

Light signals are transduced into graded potentials by photoreceptors (**R**: rod photoreceptor, **C**: cone photoreceptors) in the photoreceptor layer (**PL**). Transmission from photoreceptors to bipolar cells occurs in the outer plexiform layer (**OPL**). Bipolar cells (whose somas define the inner nuclear layer, **INL**) are broken down into two broad types: 'ON' and 'OFF' (responding to increments and decriments in illumination respectively. In this work, two types of ON bipolar cells were stimulated optogenetically (the rod bipoalr cell, **RB**; and the type-6 ON cone bipolar cell, **T6**). Release from bipolar cell terminals onto amacrine cells or ganglion cells occurs within the inner plexiform layer (**IPL**). The IPL is also subdivided into 'ON' and 'OFF' sublaminae, with ON cells forming synapses in the ON sublaminae, and OFF cells forming synapses in the OFF sublaminae. (Note that an exception to this rule will be discussed in Chapter 3.) RBs drive excitation onto AII amacrine cell neurites in the IPL. AII cells are bistratified, forming an electrical synapse with T6 cells in the ON sublaminae of the IPL, or providing glycinergic inhibition onto OFF gangion cell dendrites (**ON-**$\alpha$ /$\delta$ ) and OFF cone bipolar cell terminals. It is through the T6 terminal that rod signals reach the ON outputs of the rod bipolar pathway, the ON-$\alpha$ ganglion cells (**ON-**$\alpha$ ).

shift in the stimulus and response relationship at photoreceptors is linear, as adaptation shifts only the sensitivity of the photoreceptor and not its response characteristics (Baccus and Meister, 2002; Dowling, 2012). Rods are substantially more sensitive to light than cones, and rod responses saturate at much lower light intensities than cone responses (Dowling, 2012). As such, rods are primarily responsible for scotopic (dim-light vision), making the rod bipolar pathway the primary circuit behind vision at low light levels (Bloomfield et al., 1997; Kolb, 2005; Dowling, 2012). However, electrical coupling from rods to cones allows rods to provide information about changes in intensity directly to the cone-pathway, as well as allowing rods to serve as relays for surround-inhibition, even in mesopic and photopic conditions (Kolb, 2005; Thoreson and Mangel, 2012; Ke et al., 2014; Szikra, 2014).

### 1.1.2 Bipolar cells are the first units of the ON and OFF pathways

In the outer plexiform layer ('OPL', Figure 1), photoreceptors form a ribbon synapse onto either ON or OFF bipolar cells (which respond to either the onset or offset of stimuli respectively, Baylor, 1996). Bipolar cell somas reside in the third retinal layer, the Inner Nuclear Layer (INL). As photoreceptors are intrinsically hyperpolarizing in the presence of light, cone synapses onto OFF cone-bipolar cells use normal glutamatergic excitation (thereby making OFF cone bipolar cells depolarize to darkness, like cones, DeVries, 2000; Borghuis et al., 2014). However, ON cone-bipolar cells need to undergo a sign inversion such that they depolarize only in response to light (Baylor, 1996; Dowling, 2012). This is achieved by way of an mGluR6-driven secondary-messenger pathway that reduces a cation conductance in the cells (Dowling, 2012; Nelson and Connaughton, 2015; Martemyanov and Sampath, 2017). Rod bipolar ('RB', Figure 1) cells, the

primary post-synaptic targets of rods, only receive rod input, and are an evolutionarily newer circuit component (Kolb, 2005; Dowling, 2012, Baden et al., 2014; Baden and Osorio, 2019). However, rod bipolar cells use the same sign inversion mechanism as ON cone bipolar cells, ultimately depolarizing with graded potentials to increases in light (Thoreson and Mangel, 2012; Euler et al., 2014).

A given rod will generally form a ribbon synapse with two rod bipolar cells (Dowling, 2012). This divergence leads to amplification of visual signals (further necessitating adaptation, Demb, 2008; Demb and Singer, 2015). As release from rod terminals is tonic, the membrane potential ($V_m$) of a given rod bipolar cell effectively encodes background luminance levels experienced by its presynaptic rods (Jarsky et al., 2011). Rod bipolar cells also receive input from 35 rod photoreceptors (Behrens et al., 2016). This convergence further amplifies signals. Further, the ON-center a of rod bipolar cell extends past the width of the cells' central inputs, and the OFF-surround extends past the cells' arbors, Kolb, 2005; Dowling, 2012). Ultimately, the terminals of rod bipolar cells form dyad ribbon synapses with two amacrine cell types, the bistratified AII amacrine cell, and the wide field A17 amacrine cell (Nelson and Kolb, 1985; Tsukamoto and Omi, 2013).

The AII amacrine cell is a narrow-field amacrine cell that relays signals into both the ON and OFF pathways, each in functionally distinct sublaminae of the Inner-Plexiform Layer ('AII', Figure 1, Kolb and Famigletti, 1974; Helmstaedter et al., 2013). Each rod bipolar cell forms synapses with approximately five AIIs (making multiple synapses with each, Demb and Singer, 2012; Ke et al., 2014). Signals also converge onto a single AII from approximately twenty rod bipolar cells (Dunn et al., 2006, 2008). In turn, AIIs are far more sensitive to increases in illumination as compared to their upstream partners. In turn, AII responses saturate more readily,

further necessitating adaptation at the rod bipolar cell to AII synapse (Jarsky et al., 2011; Demb and Singer, 2012).

### 1.1.3 The RB→AII/A17 Synapse

Rod bipolar cell membrane potential ($V_m$) has a direct relationship with the signal-to-noise ratio (SNR) of transmission to post-synaptic AII amacrine cells (Jarsky et al., 2011; Ke et al., 2014). As RB $V_m$ determines the rate of background vesicle release, SNR of the synapse is reduced in depolarized states (Jarsky et al., 2011; Ke et al., 2014). When the rod bipolar terminal is depolarized, the strength of transmission at the rod bipolar cell to AII synapse is also reduced (in part due to inactivation of $Ca^{2+}$ currents, Jarsky et al., 2011). When the rod bipolar cell terminal is hyperpolarized (as in dark conditions), the rod bipolar to AII synapse shows facilitated transmission, shifting to encode contrast (Ke et al., 2014). Transmission at the rod bipolar terminal is ribbon-mediated, also adding to its high fidelity (high SNR) nature (Lagnado, 2003; Jarsky et al., 2010). These features suggest a mechanism for gain control at the rod bipolar to AII synapse, likely reliant on synaptic depression (via depletion of the readily releasable pool of vesicles, which is further outlined later, Singer and Diamond, 2006; Dunn et al., 2006; Demb and Singer, 2015).

AIIs also communicate with each other through direct, homologous (non-rectifying) gap junctions (Vardi and Smith, 1996; Veruki and Hartveit, 2002a, 2002b; Veruki et al., 2008, 2010; Demb and Singer, 2012, 2015; Choi et al., 2014). AII-AII gap junction coupling is controlled by dopaminergic modulation onto AII somas (from Dopaminergic Amacrine Cells, 'DACs'/A18s, which form rings of synapses around each AII (Hampson et al., 1992). While coupled under

scotopic (low light) conditions, weak signals from one AII may pass laterally to others, thereby amplifying the signal and averaging out noise (Texler et al., 2001; Bloomfield and Völgyi, 2004). Without this mechanism, noise would otherwise be a serious problem for sparse signals of low intensity. In photopic conditions, decoupling prevents saturation in this circuit, allowing finer spatial discriminability. This has been proposed as a mechanism for adaptation within the AII circuit (Hampson et al., 1992; Bloomfield and Völgyi, 2004).

Concurrently, the A17 (a functionally atypical wide-field amacrine cell) forms a recurrent synapse onto the RB terminal. This synapse uses a seemingly unique mechanism for GABAergic transmission. When a glutamatergic signal from a rod bipolar cell reaches the A17, it leads to the opening of $Ca^{2+}$ permeable AMPA receptors. The influx of $Ca^{2+}$ is rapid, leading to the release of an intracellular store of additional $Ca^{2+}$ ions (Chávez et al., 2006). Release of GABA is constrained locally to a given synapse, with minimal signal conduction between A17 varicosities (unlike most wide-field amacrine cells, Menger and Wassle, 2000; Grimes et al., 2010; Diamond and Grimes, 2014; Grimes et al., 2015). Depolarization of the A17 will then drive release of GABA-containing vesicles, thereby hyperpolarizing the rod bipolar cell terminal. Rod bipolar cell terminal hyperpolarization in turn facilitates vesicular release by its ribbon terminal (Hartveit, 1999; Dong and Hare, 2003; Chávez et al., 2006; Diamond and Grimes, 2014).

## 1.2 General methods for assessing temporal contrast adaptation

Given the extensive adaptive processes throughout the outer retina (some mentioned previously), using conventional light-stimulation would make it difficult to attribute adaptation to individual components of the circuit (Chapot et al., 2017a, 2017b). Further, most retinal ganglion cells

receive presynaptic input from multiple circuit types (with fifteen different bipolar cells, each with distinct receptive field properties, Euler and Masland, 2000; Roska and Werblin, 2001; Euler et al., 2014; Shekhar, 2016; Baden et al., 2013). As such, methods for ablating input from the outer retina and directly targeting the rod bipolar pathway are necessary. The remainder of this chapter focuses on methods to isolate the rod bipolar pathway and how to examine the processes of adaptation that occur within it.

### 1.2.1 Retinal extraction and whole-cell patch clamp recordings

First, retinas were extracted from the enucleated eyes of adult mice ($\geq$ 35 days old) in a bicarbonate-buffered Ames' Solution (Sigma). Retinal whole-mounts were created by mounting excised tissue from ventral retinas onto hole-punched nitrocellulose paper. Whole-mounts were immediately transferred to a recording chamber with a bicarbonate-buffered standard external solution, heated to 31-34°C. Fresh, temperature-controlled and pH buffered external solution was continually flowed through the recording chamber via a peristaltic pump, and removed using vacuum suction. Retinas were allowed to sit in the recording chamber for a minimum of five minutes before recordings were attempted (to increase mechanical stability).

Voltage clamp recordings were collected using a $Cs^+$-based internal solution containing QX-314 chloride (an internal $Na_v$ blocker, ToCris/Cayman) in patch electrodes ($\sim$4-7M$\Omega$ resistance for AIIs and ganglion cells, $\sim$10-12M$\Omega$ resistance for bipolar cells). This allowed for recordings of EPSCs at an $E_{Cl} \approx$ -67mV, and IPSCs at a holding potential $\approx$ 0mV. Most cells were also loaded with Alexa Flour 488 Hydrazide (Thermo-Fisher), to allow for post-recording confirmation of cell type. Initially, data were collected on an Axon Instruments Multiclamp 700B amplifier

with an Instrutech digitizer. During the course of experiments, we switched to a newer Sutter Instruments d-IPA (dual-headstage Integrated Patch Amplifier), which served as both amplifier and digitizer for most of this work. Recordings were initially collected using custom-written code (in Igor) from the Singer Lab. With the transition to the d-IPA amplifiers, we switched to Sutter's SutterPatch software (also built in Igor). To facilitate analysis of data from these two different systems, all data were ultimately exported and processed using Matlab code written by the author.

### 1.2.2 Optogenetic stimulation of the rod bipolar pathway

Cre-mediated, YFP-linked channelrhodopsin-2 (ChR2) expression was targeted to either rod bipolar cells or type-6 ON cone bipolar cells. Initially, two strains of mice were used for RB targeting, L7Cre and PCP2Cre. However, L7Cre mice showed slight off-target expression of ChR2 in ON cone bipolar cells, while expression was more reliably limited to rod bipolar cells in PCP2Cre mice. As such, data shown here are exclusively from PCP2Cre line. In the case of type-6 ON cone bipolar cell targeting, we used the CCKcre mouse line. All Cre lines were crossed with the Ai32 reporter line. This allowed for direct stimulation of a specific bipolar cell types with 470nm blue light.

ChR2 was excited using temporally varying white noise stimuli projected from one of three 470nm LEDs (ThorLabs). For early experiments, this LED was embedded in a Zeiss Axioskop 2FS microscope. Later experiments (after May 2020) were performed using a custom-built microscope using the ThorLabs Cerna platform (ThorLabs, in an effort to maintain social distancing). LEDs and their drivers were changed during the course of experiments due to failures

or when switching recording systems. In each case, LEDs were calibrated, and the linearity of light presentation was confirmed prior to further data collection. All stimuli included a small offset to account for the minimum voltage required to drive the LED (≈200mV, with slight variation between LED drivers). To minimize error introduced by the subtle variability in this offset, stimuli were passed through a neutral density filter (with optical density of 0.5 for PCPcre experiments, or optical density of 0.9 for CCKcre experiments, ThorLabs). This also allowed stimuli to vary over the maximum operating range of the LEDs and their drivers (also from ThorLabs).

Stimuli were presented through a 60X water-immersion lens (Olympus/Nikon). In whole mount preparations, stimuli were manually focused onto the INL (which can easily be identified by somatic YFP-expression in our mouse lines). In slice preparations, light was focused directly onto the bipolar cell somas. The stimulus system was initially calibrated using an OceanOptics USB4000 spectrophotometer on loan from Dr. Karen Carleton (UMD). Later, a ThorLabs light power meter was used.

### 1.2.3 Constructing Linear-Nonlinear models

Linear-Nonlinear (L-N) Cascade Models are useful tools for studying contrast adaptation and receptive field structure (Chichilnisky, 2001; Zaghloul et al., 2003; Jarsky et al., 2011). They are particularly useful for characterizing circuits using 'naturalistic' stimuli, and have been a frequently used tool to study retinal receptive fields (Chichilnisky, 2001; Zaghloul et al., 2003; Jarsky et al., 2011). In this work, L-N models were constructed using a Gaussian white noise stimulus generated by temporally modulating light intensity around a background mean.

Peak illumination was set to the point of saturation of response for each target for optogenetic stimulation (that is, specific to each Cre line). Background mean was set to the half-max amplitude of a saturating response. This allowed us to characterize the full operating-range of each circuit component that we examined. Most stimulus sequences were first created in Matlab, and subsequently imported to the Igor-based acquisition systems mentioned previously.

A linear kernel ($k$) can be estimated by cross-correlating the stimulus and recorded response (this process is illustrated in Figure 2, Wiener, 1949, 1958; Lee and Schetzen, 1965; Marmarelis and Marmarelis, 1978; Zaghloul et al., 2003; Beaudin et al., 2008; Demb, 2008; Jarsky et al., 2011). In this work, a unique stimulus sequence can be cross correlated with its corresponding response (Figure 2, red). Frequently, this kernel is estimated after deconvolving the crosscorrelogram with the autocorrelogram of stimulus. Following previously established procedures in the lab, though that step was excluded here (Cembrowski, 2011). Conceptually, the linear kernel (Figure 2, '$k$') is a representation of the temporal characteristics of the system's response. The filtered stimulus can then be passed through a static nonlinearity to generate a model prediction. Meanwhile, the nonlinearity ($N$) accounts for a number of nonlinear components throughout the circuit, and maps a generator signal (g($t$) onto the recorded outputs of the circuit. (Note that the generator signal, g($t$), is estimated by convolving the stimulus with the cross correlogram.) Several examples of sources for the nonlinearity include: rectification through synaptic release and response saturation (Jarsky et al., 2011). Conceptually, the nonlinearity is effectively a gain function for the circuit (Chichilnisky, 2001; Cembrowski, 2011). By equating the nonlinearities between contrast conditions, linear kernels can then be re-scaled. Gain change between conditions can then be measured as the relative difference of the peaks of the two re-scaled linear filters. For ease of display, this dissertation uses relative gain as the measurement for gain change (that is, the amplitude of

the low contrast filter normalized to the peak of its corresponding high contrast filter, Figure 2, 'relative gain', *center*). Finally, model quality can be measured using the embedded test sequences within a white noise stimulus (Figure 2, blue). These test sequences can be compared to model fits, generating an estimate of the variance explained by the model ($r^2$ of L-N fit).

For the experiments throughout this dissertation, white noise stimuli were generated as follows. A brief sequence of 'no-stimulus' was followed by an initial 'background' illumination (with amplitude set to evoke a half-max response, scaled for each Cre line). This background was projected for four seconds, allowing the response to reach a steady state. The background segment was then followed by Gaussian noise stimuli varied about the mean background (Figure 2, *top*). Most noise sequences consisted of six segments of ten second duration. (Exceptions are discussed in a Chapter 4 of this dissertation).

Individual segments alternated between high and low contrast (as can be seen in Figure 2, *top*). High contrast segments were set to extend over the full operating range of the circuit (from no-light to saturation), while low contrast segments were set with a standard deviation $\frac{1}{3}^{\text{rd}}$ that of the high contrast segments. Segments were concatenated into an individual noise sequence, altering between high and low conditions. These noise sequences were then bandpass filtered from 0-20Hz (to keep stimulation within the operating time course of channelrhodopsin-2, Zhang et al., 2006). Each segment consisted of 7-8 seconds of unique noise stimulation, and 2-3 seconds of repeated noise sequences. Thereby, each stimulus 'sweep' (the background stimulation and subsequent noise sequence) consisted of 21-24 seconds of unique stimulation, and 6-9 seconds of repeated stimulation for each of two conditions (high and low contrast). Contrast presentation order (high→low or low→high contrast) was counterbalanced between sweeps (Figure 2, *top*, shows a high→low presentation order). This resulted in two stimulus sweeps of 64 second total

'up-time' duration. Both stimulus sweeps had distinct unique noise sequences. Inter-sweep interval was set to 120 seconds, to account for ChR2 kinetics and reduce rundown (Zhang et al., 2006; Schneider et al., 2015).

Recording data from unique sequences were concatenated between sweeps, with 360ms excised surrounding each transition point (180ms in each direction around transitions between contrast condition, or between unique and repeat segments). These transition-proximal data were excluded to minimize the impact of non-random sequences on model construction (Victor, 1992; in: Pinter and Nabet, 1992; Chichilnisky, 2001). This method accounts for some of the non-random structure of the stimulus sequence, thereby helping to maintain orthogonality of stimulus values at each time point (a major assumption of white noise-based methods, Chichilnisky, 2001). Further, this also counters some of the problems with excluding the autocorrelogram deconvolution step when estimating kernels (as in Cembrowski, 2011). The isolated 'unique' data were used to generate the models shown throughout this dissertation. Recordings from repeated sequences were averaged and used to test model predictions. Finally, individual repeat sequences were used as an ongoing quality-check within each stimulus-response sweep. This allowed us to exclude segments of data with significant rundown of the ChR2 response, and is discussed further in Chapter 4.

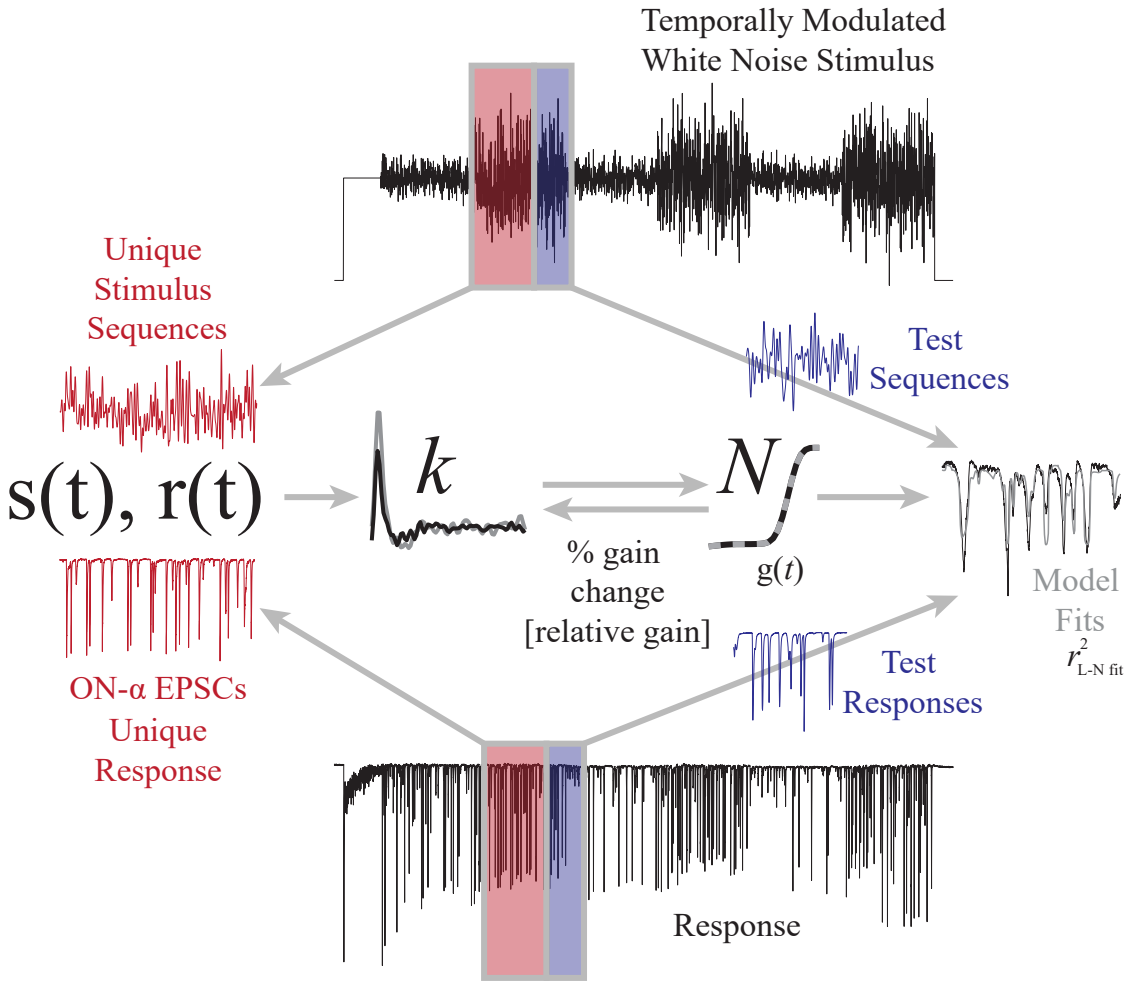


Figure 1.2: Schematic of L-N cascade modeling

For multiple experiments throughout this dissertation, a Gaussian white noise stimulus (modulated about a background mean illumination level) was used to drive channelrhodopsin-2 in targeted bipolar cell types. Stimulus sweeps contained two contrast conditions (visible in the *top* trace). Within each contrast segment, a unique sequence (red) was used to build L-N models, while a repeated sequence (shared between different segments of a given contrast condition) was used to test those models. From the stimulus 's(t)' and corresponding response 'r(t)', a linear kernel can be estimated ($k$, *center*). That kernel can then be used to estimate the generator signal, g($t$) (*center*), which allows for estimation of the nonlinearity ($N$) for each contrast condition. By equating the nonlinearities between conditions, we can re-scale the kernels. The end result of that process yields the percent gain change as the difference between the peak amplitudes of filter peaks for the two contrast conditions. Finally, a model fit ($r^2$) can be generated and compared to the averaged repeat sequences (*right*).

# Chapter 2: Isolating adaptation in the ON component of the rod bipolar pathway

The first section of this chapter discusses experiments to examine how well we could optogenetically drive bipolar cells over physiological ranges. The second section begins examining downstream synaptic components of contrast adaptation (adaptation via synapses onto AII amacrine cells, then adaptation onto the output of the ON component of the rod bipolar pathway:ON-$\alpha$ ganglion cells). The third section show results examining a possible source for the synaptic mechanisms of gain control that we observed–that being the dynamics of the readily releasable pool of vesicles. In the fourth section we characterize the effects of the AII membrane potential in shaping how adaptation occurs within the pathway. In the final section, this chapter closes with a discussion of these findings, and what they might mean for the overall function of the rod bipolar pathway.

## 2.1 Optogenetic stimulation of bipolar cells

Before examining downstream circuit components, we first needed to confirm that ChR2 could drive bipolar cells in a physiologically plausible manner.

We prepared retinal slices from mice expressing ChR2 in each of the target bipolar cell types of the rod bipolar pathway. All other methods were comparible to the whole-mount preparation methods outlined in section 1.2.1 of this dissertation. ChR2-expressing bipolar cells were targeted

for patching using their YFP label. Cells were patched in either current clamp, or voltage clamp. Current clamp recordings allowed us to examine whether the membrane potential of each bipolar cell adapted to optogenetic stimulation. Meanwhile, voltage clamp recordings (held at the chloride reversal potential, $E_{Cl}$), allowed us to examine whether channelrhodopsin currents adapted to shifts in contrast. White noise stimuli were presented to the patched bipolar cells, and Linear-Nonlinear models were constructed from their response data.

### 2.1.1 Bipolar cell control results

Figure 2.1 shows the L-N modeling results of an example rod bipolar cell, patched in slice from a PCP2creAi32 mouse, and recorded in current clamp. **A** shows a schematic of the rod bipolar pathway that will be used frequently throughout this dissertation. In this case, a rod bipolar cell is patched in whole cell current clamp ('RB', green) and stimulated with a 470nm LED ('RB', blue). **B** shows a full white noise stimulus sequence as presented to this cell (showing alternating contrast conditions). Note that the stimulus amplitude is scaled to saturation here. **C** shows the corresponding response (membrane potential) of the patched rod bipolar cell in response to the stimulus in **B**. Horizontal axes (time) are shared between **B** & **C**. Meanwhile, **D** shows the re-scaled linear kernels (*k*, dark blue: high contrast condition, light blue: low contrast condition), with re-scaled nonlinearities (*N*, insert). Meanwhile, **E** & **F** show a one second long portion of the repeated noise sequence (gray), its corresponding average response (black), and L-N model fits (dark blue, *top*, for high contrast, and light blue, *bottom*, for low contrast). In the cases of membrane potential and IPSC recordings throughout this dissertation, the stimulus sequence is inverted to align with the response sequence in these

sub-figures. Further, all three traces (stimulus, average response, and L-N model prediction) are $z$-transformed, for visualization purposes. As noted in Figure 1.2, repeated noise sequences were embedded within the larger white noise sequence. No significant difference was observed in gain between contrast conditions for rod bipolar cell membrane potentials when stimulated with ChR2 ($n$ = 7, $t_{\text{one-sample}}(6)$ = -1.293, $p$ = 0.2419, mean relative gain = 0.96 $\pm$0.033).

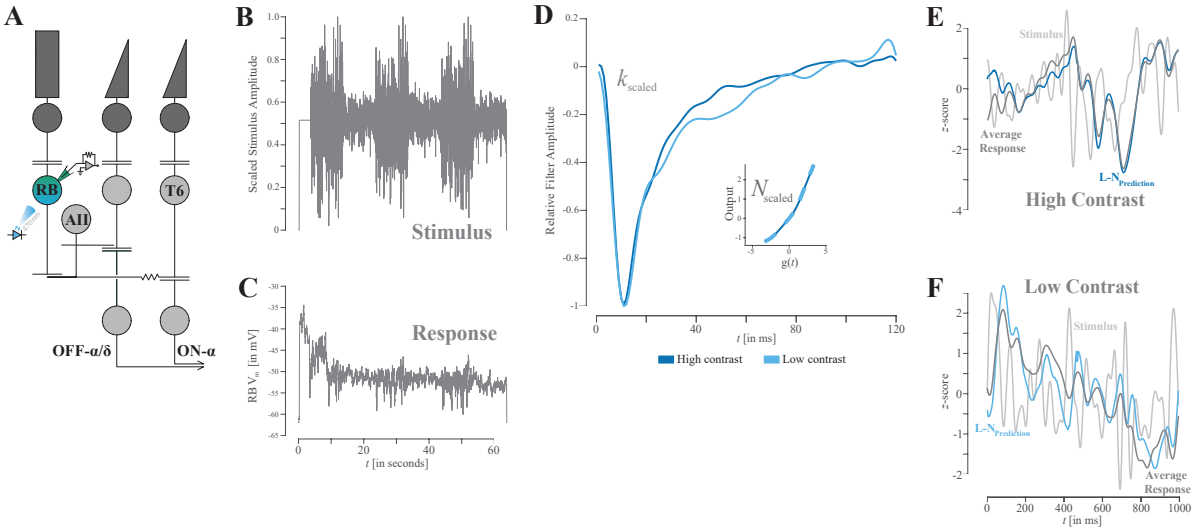


Figure 2.1: Example data for a rod bipolar cell showing no adaptation in membrane potential ($V_m$)
**A**: schematic of the rod bipolar pathway, showing a rod bipolar cell (**RB**) being recorded from (green) and optogenetically stimulated (blue). **B**: an example stimulus sweep, scaled to saturation and fluctuating around a mean value set to the half-max response amplitude. **C**: Corresponding $V_m$ trace recorded from a rod bipolar cell in whole cell current clamp, corresponding to the stimulus shown in **B**. **D**: the re-scaled linear kernels for the two contrast conditions, with scaled nonlinearities *insert*. The equal peak amplitudes between the re-scaled kernels shows that there is no gain change between the two contrast conditions in this figure. **E**: a zoomed-in depiction of stimulus (gray), mean response (black) and L-N model fit (dark blue) for a high contrast repeat segment, with values $z$-transformed (for easier visualization). **F**: as **E**, but for low contrast (with L-N model fit shown in light blue).

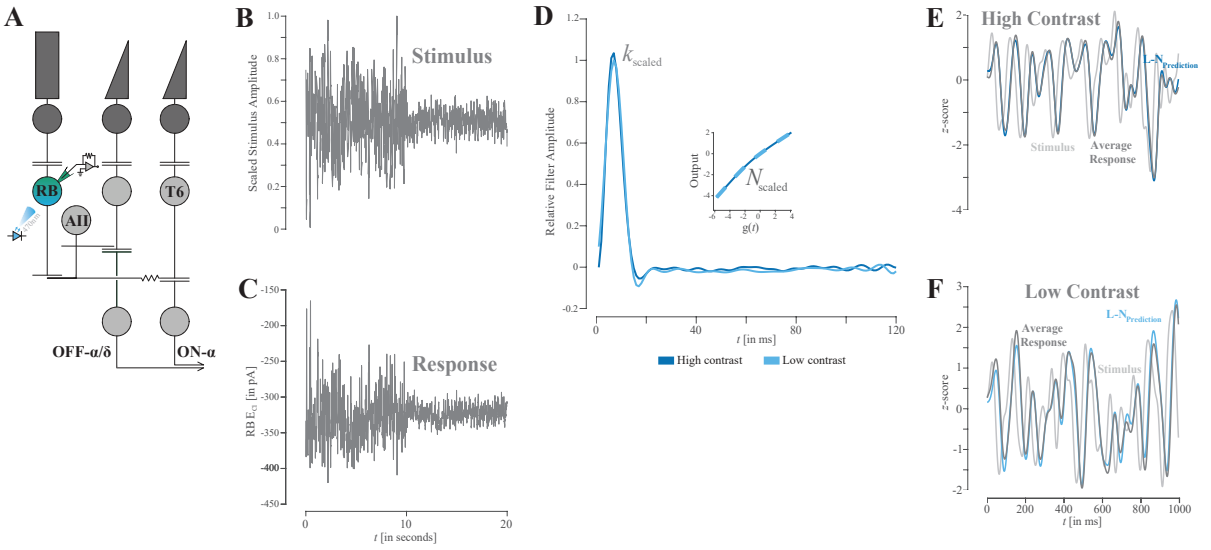


Figure 2.2: Example data for a rod bipolar cell showing no adaptation in ChR2 currents (held at $E_{Cl}$)

**A**: schematic of the rod bipolar pathway, showing a rod bipolar cell (**RB**) being recorded from (green) and optogenetically stimulated (blue). **B**: an example stimulus, focused on two difference contrast segments, scaled to saturation and fluctuating around a mean value set to the half-max response amplitude. **C**: Corresponding ChR2 currents recorded from a rod bipolar cell in whole cell current clamp (held at $E_{Cl}$), corresponding to the stimulus shown in **B**. **D**: the re-scaled linear kernels for the two contrast conditions, with scaled nonlinearities *insert*. The equal peak amplitudes between the re-scaled kernels shows that there is no gain change between the two contrast conditions in this figure. **E**: a zoomed-in depiction of stimulus (gray), mean response (black) and L-N model fit (dark blue) for a high contrast repeat segment, with values $z$-transformed (for easier visualization). **F**: as **E**, but for low contrast (with L-N model fit shown in light blue). Note the high coherence between stimulus, ChR2 currents, and L-N model fits in **E** & **F**.

Figure 2.2 shows data collected by recording from a rod bipolar cell in slice from a PCP2creAi32 mouse. However, these recordings were collected in voltage clamp, at $E_{Cl}$, allowing one to assess whether the ChR2 currents themselves adapted. No gain change was observed for these conditions either (mean relative gain = 1.01 $\pm$0.037). Note that **B** & **C** both focus on only one iteration of a contrast condition. Additionally, the example traces in **E** & **F** both show the response and model prediction clearly following the stimulus sequence.

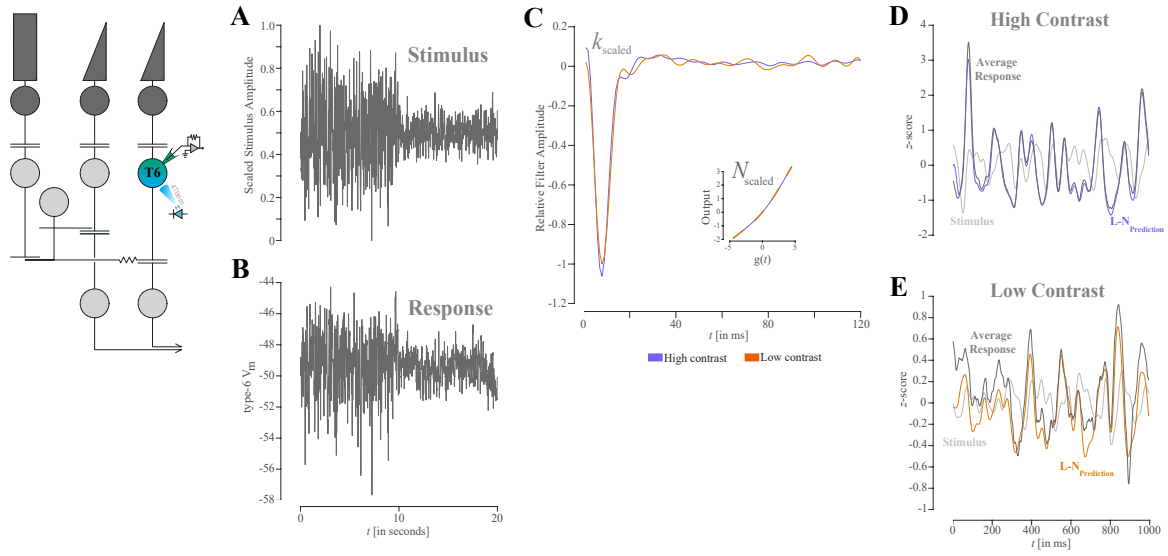


Figure 2.3: Example data for a type-6 ON cone bipolar cell showing no adaptation in membrane potential ($V_m$)
**A**: schematic of the rod bipolar pathway, showing a type-6 ON cone bipolar cell (**T6**) being recorded from (green) and optogenetically stimulated (blue). **B**: an example stimulus, focused on two difference contrast segments, scaled to saturation and fluctuating around a mean value set to the half-max response amplitude. **C**: Corresponding type-6 $V_m$ response to the stimulus shown in **B**. **D**: the re-scaled linear kernels for the two contrast conditions, with scaled nonlinearities *insert*. High contrast is shown in purple, while low contrast is shown in orange. The equal peak amplitudes between the re-scaled kernels shows that there is no gain change between the two contrast conditions in this figure. **E**: a zoomed-in depiction of stimulus (gray), mean response (black) and L-N model fit (purple) for a high contrast repeat segment, with values *z*-transformed (for easier visualization). **F**: as **E**, but for low contrast (with L-N model fit shown in orange).

Figure 2.3 shows L-N modeling results for a type-6 ON cone bipolar cell, patched in slice from a CCKcreAi32 mouse, and recorded in current clamp (with a schematic of the circuit, *left*). The first contrast condition presentations of white noise stimulus sequence presented using a 470nm LED (**A**) and response (**B**). Concurrently, **C** shows the re-scaled linear kernels (*k*, purple: high contrast condition, orange: low contrast condition), with re-scaled nonlinearities (*N*, *insert*). Further, both **D** & **E** show a repeated noise stimulus sequence (black), and either a high contrast (dark purple, top), or low contrast (orange, bottom) averaged response. No significant difference was observed in gain between contrast conditions for type-6 ON cone bipolar cells either ($n$ = 14, $t(13)$ = -2.0024, $p$ = 0.0541, mean relative gain = 0.96 $\pm$0.02). Note that many of these recordings showed increased noise, leading to ripples in the linear filters. At least some of this is due to the spiking of electrically coupled AII amacrine cells. Similar voltage clamp recordings were attempted, but the spiking activity of the AII network led to unclamped action currents, making it impossible to estimate postsynaptic currents reliably. Further, those recordings were also subject to an equipment failure that will be discussed in Chapter 4.

Figures 2.4, 2.5, & 2.6 show a series of scatter plots that show the relationship between the L-N model fits ($r^2$ values) for the two contrast conditions used in this work (*left*), or (*center* & *right*) the relative gain as a function of model fits for each contrast condition (low contrast *center*, high contrast *right*). In Figure 2.4, observe the positive correlation between model fits for the two contrast levels, as well as the statistically insignificant relationship between model fits for each contrast condition and the overall relative gain estimate. A positive $r^2$ value for the model fits between contrast conditions suggests covariance and supports the claim that any measured differences in gain are not a confound of poor model fits for an individual condition. Meanwhile, the insignificant $r^2$ value for the relative gain and each contrast condition further suggests that

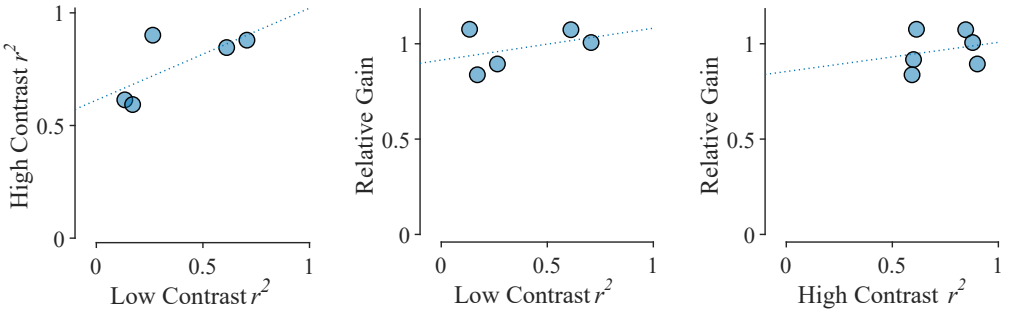


Figure 2.4: Relative gains and L-N model fits ($r^2$) for rod bipolar cell $V_m$ recordings ($V_m$)
These figures show the relationship between L-N model fits for each contrast condition ($r^2$), as well as the estimated relative gain change for rod bipolar cell Vm recordings. *Left* shows the positive relationship between the model fits for the two contrast conditions (suggesting that variability in model fit is a function of the individual cell recorded, *not* the contrast condtion. *Center* & *right* show the poor relationship between relative gain estimate and the model fits for each contrast condition; suggesting that our gain estimates were not overly influenced by the quality of the model fits for one contrast condition over the other.

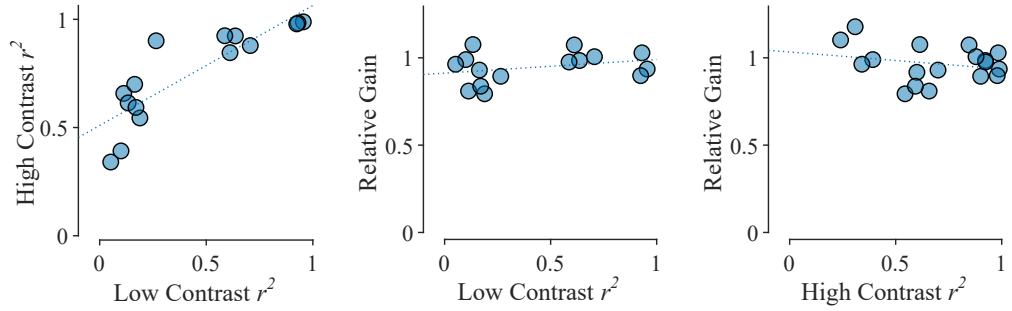


Figure 2.5: Relative gains and L-N model fits ($r^2$) for ChR2 currents on rod bipolar cells recordings (held at $E_{Cl}$)
These figures show the relationship between L-N model fits for each contrast condition ($r^2$), as well as the estimated relative gain change for ChR2 currents recorded from rod bipolar cells (held at $E_{Cl}$). *Left* shows the positive relationship between the model fits for the two contrast conditions (suggesting that variability in model fit is a function of the individual cell recorded, *not* the contrast condtion. *Center* & *right* show the poor relationship between relative gain estimate and the model fits for each contrast condition, suggesting that our gain estimates were not overly influenced by the quality of the model fits for a individual contrast condition. Note the faint clustering into two groups. This is likely due to necessary data corrections that are discussed in Chapter 4, and can often lead to reduced L-N model fit ($r^2$) values.

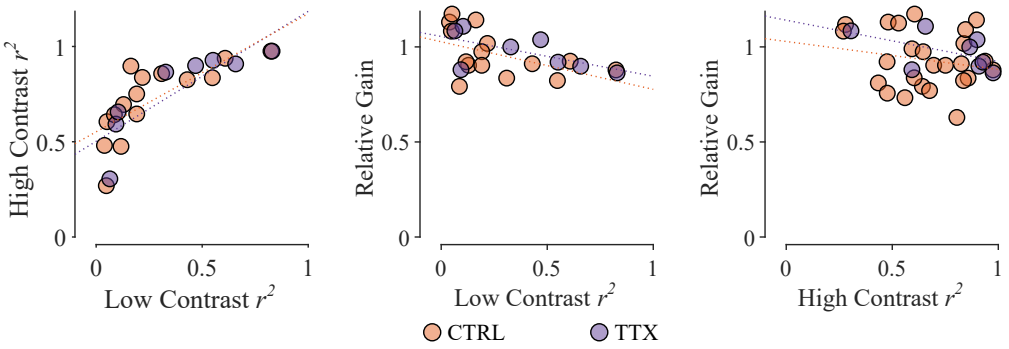


Figure 2.6: Relative gains and L-N model fits ($r^2$) for type-6 ON cone bipolar cell membrane potential recordings ($V_m$)
These figures show the relationship between L-N model fits for each contrast condition ($r^2$), as well as the estimated relative gain change for the $V_m$ recorded from type-6 bipolar cells stimulated by ChR2. Orange points indicate type-6 ON cone bipolar cells in a standard external solution, while purple points correspond to recordings in the presence of TTX. The reason for this is discussed in the text, and relates to the troubleshooting discussed in Chapter 4. *Left* shows the positive relationship between the model fits for the two contrast conditions (suggesting that variability in model fit is a function of the individual cell recorded, *not* the contrast condition). *Center* & *right* show the poor relationship between relative gain estimate and the model fits for each contrast condition; suggesting that our gain estimates were not overly influenced by the quality of the model fits for either contrast condition.

neither contrast condition is contributing more than the other for shaping the model. Figures 2.4 and 2.5 correspond to rod bipolar cell membrane potential, and channelrhosopsin-2 current recordings respectively. Figure 2.6 follows the same overall structure, however it includes data collected in the presence of TTX [500nM]. These data were collected in an effort to improve model fits for type-6 ON cone bipolar cells. At the time, we believed the model fits were poor due to unclamped spikes from AIIs coupled to the type-6 cells we were patching. It later became clear that we were also dealing with a hardware-related issue that will be discussed in Chapter 4.

Figure 2.7 shows an aggregate of the relative gain measured from multiple control recording types from bipolar cells expressing ChR2. This figure shows relative gain measurements for cells patched in voltage clamp and held at either $E_{Cl}$ or $E_{cation}$. Note that recordings for type-6 ON cone bipolar cells are omitted. The difference between cell types in the $E_{Cl}$ condition is not

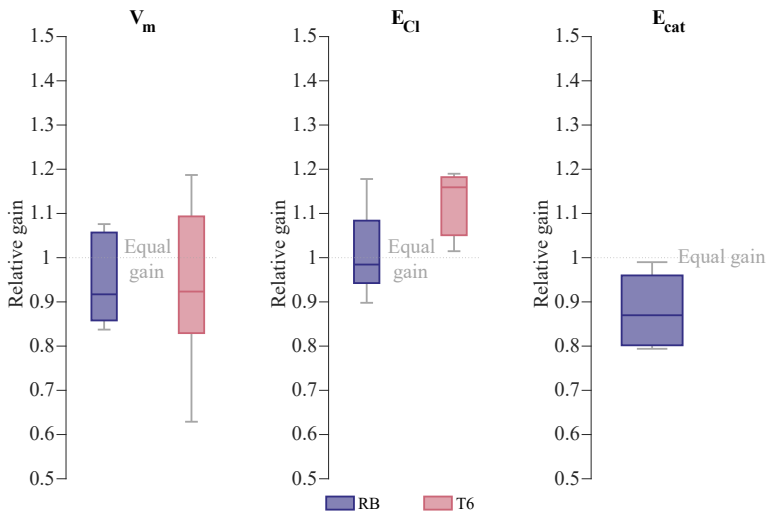


Figure 2.7: Aggregate gain estimates for rod bipolar cells and type-6 ON cone bipolar cells
The boxplots shown here are for the relative gain estimates for each bipolar cell type (rod bipolar cells in purple, type-6 ON cone bipolar cells in pink). *Left* shows the equal gain between both contrast conditions seen tin the membrane potential. *Center* shows the results for ChR2 currents recorded from both bipolar cell type. Note that while it may seem there is a faint gain change present in type-6 data, the effect is insignificant. Further, those recordings did not yield good model fits (for reasons covered in the Discussion section). Finally, *right* shows the relative gain estimates for feedback inhibition onto bipolar cells. Type-6 data were not included in this figure, for reasons discussed in the text.

| | | Gain Est. | | *t*-tests | | |
|---|---|---|---|---|---|---|
| | *n* | Mean relative gain | S.E.M. | *t*(*df*) | *p* | $CI_{95\%}$ |
| rod bipolar cell $V_m$ | 7 | 0.96 | ±0.033 | *t*(*6*) = 1.30 | *p*=0.24 | 0.86:1.05 |
| type-6 ON cone bipolar cell $V_m$ | 15 | 0.96 | ±0.02 | *t*(*14*) = 2.00 | *p*>0.05 | 0.89:1.00 |
| rod bipolar cell ChR2 currents | 7 | 1.01 | ±0.037 | *t*(*6*) = 0.35 | *p*=0.74 | 0.92:1.10 |

Table 2.1: Gain change estimates and statistical results for bipolar cell control experiments
Stimulus sources and recording types are listed in the first column. Sample sizes are listed in the second column. Relative gain (second column) is estimated by normalizing both linear kernels to the peak amplitude of the high contrast kernel, then taking the peak amplitude of the low contrast kernel, with standard error of the mean included (third column). One-sample *t*-tests were used to estimate if any observed differences in relative gain were significant versus equal gain (that is, relative gain equal to one). Confidence intervals (95%) were also measured for the relative gain estimates, and are shown in the final column.

statistically significant ($p>0.05$). Additionally, recordings from type-6 cells held at $E_{cat}$ were omitted (as noted previously). No significant gain changes were measured at the bipolar cells in any of these recording types or conditions. A summary of these control experiments and their statistics can be found in Table 2.1.

## 2.2 Synaptic sources of adaptation in the ON component of the rod bipolar pathway

### 2.2.1 Sources of adaptation onto AII amacrine cells

L-N model results show an increased relative gain for AII amacrine cells held at $E_{Cl}$ in response to up-stream optogenetic stimulation of rod bipolar cells (elaborated on below). This indicates that the synapse from rod bipolar cells to AII amacrine cells is the earliest site of contrast adaptation. Note that filters are slower than those seen previously (as in Jarsky et al., 2011). This is due to the kinetics of channelrhodopsin-2 and is a limitation of its use.

The relative gain estimates for signals reaching AII amacrince cells stimulated by either rod bipolar cells (blue) or cone bipolar cells (brown) expressing ChR2 are shown in Figure 2.8. Please note the two outliers in the AII EPSC data (*left*). Nether cell had clear indications as to why one might remove their data (other than the increased gain change). As such, they were included in this figure. Further, their removal does not change the outcome of any hypothesis testing. No gain change was observed when driving AIIs through their gap junction with type-6 ON cone bipolar cells ($n$ = 18, $t(17)$ = -0.51, $p$ = 0.619, $CI_{95\%}$ = 0.87:1.08, mean relative gain = 0.98 $\pm$0.049). With rod bipolar cell stimulation, a gain change did occur with excitation (AIIs held at $E_{Cl}$, $p$ <0.001, $CI_{95\%}$ = 1.29:1.60, mean relative gain = 1.40 $\pm$0.092, see Figure 2.8, **D** for an example of the scaled kernels). Interestingly, no gain change was observed in inhibition back on to AIIs during rod bipolar cell stimulation. In fact, feedback inhibition onto the AIIs appears to sensitize (that is, showing a relative gain for low contrast less than one). However, the effect is not statistically significant ($n$ = 15, $t(14)$ = -0.39, $p$ = 0.704, $CI_{95\%}$ = 0.50:1.35, mean relative gain

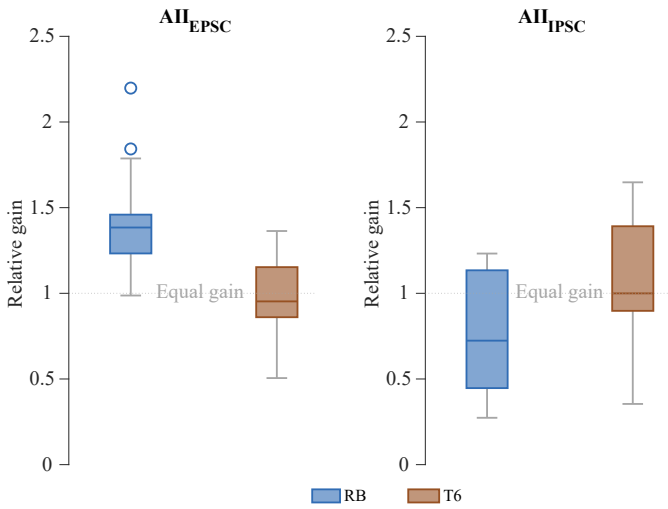


Figure 2.8: AII relative gain estimates as a function of optogenetic stimulus source
The boxplots shown here are for the relative gain estimates for postsynaptic currents recorded from AII amacrine cells for each optogenetic stimulus source (rod bipolar cells in blue, type-6 ON cone bipolar cells in brown). *Left* shows the increased relative gain for excitation onto AIIs when driven by rod bipolar cells (blue). *Right* shows the relative gain estimates for feedback inhibition onto AII amacrine cells. No gain change was observed to reach AIIs from type-6 stimulation, or feedback inhibition.

= 0.92 ±0.20). Given the variability in the relative gain recorded from AIIs in $E_{cat}$ during type-6 ON cone bipolar cell stimulation, it is possible that an effect is being masked by action currents from AIIs coupled to the ones recorded here.

Figures 2.9 and 2.10 show model quality checks by comparing the L-N model fit for two contrast conditions with the relative gain at two holding potentials (Figure 2.9 at $E_{Cl}$, Figure 2.10 at $E_{cat}$). For both figures, rod bipolar stimulation is shown with blue dots, and type-6 ON cone bipolar stimulation is shown with orange dots. (*left*) shows the comparison of the two contrast conditions. The positive correlations of fit quality for both conditions suggests that any observed effects are not due to differences of fit quality between the conditions ($r^2$=0.76, $p$ <0.001). Additionally, (*center* & *right*) show the relationship between model fits for each contrast condition and the relative gain. No significant relationship was observed, indicating that relative gain estimates are not biased toward the contribution of either contrast condition to the model ($r^2$ = 0.23 & 0.001, $p$ = 0.35 & 0.99 for low and high contrast respectively).

### 2.2.2 Contrast adaptation is limited to the excitatory inputs to ON-α ganglion cells originating from rod bipolar cell stimulation

Recordings in Figure 2.11 were collected from an ON-α retinal ganglion cell during optogenetic stimulation of upstream rod bipolar cells (illustrated in **A**). **B** shows a single stimulus presentation of each contrast condition, while **C** shows the corresponding response. **D** shows the re-scaled linear kernels (*k*), and nonlinearities (*N*, *inset*). Finally, **E** & **F** both show a shorter repeat stimulus sequence (gray), corresponding averaged response trace (black), and corresponding model fits (red)(dark blue: high contrast, light blue: low contrast). A significant gain change is observed

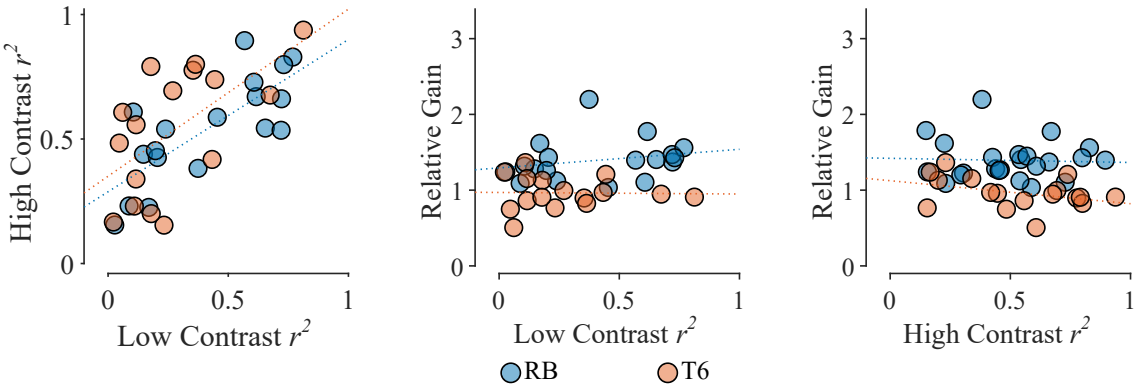


Figure 2.9: AII $E_{Cl}$ model fits ($r^2$) and relative gain

These figures show the relationship between L-N model fits for each contrast condition ($r^2$), as well as the estimated relative gain change for excitatory currents onto AII amacrine cells. Blue points correspond to optogenetic stimulation of rod bipolar cells, while orange points indicate type-6 ON cone bipolar cells as the stimulus source. *Left* shows the positive relationship between the model fits for the two contrast conditions for both stimulus sources (suggesting that variability in model fit is a function of the individual cell recorded, *not* the contrast condition). *Center* & *right* show the poor relationship between relative gain estimate and the model fits for each contrast condition; suggesting that our gain estimates were not overly influenced by the quality of the model fits for one contrast condition of another.

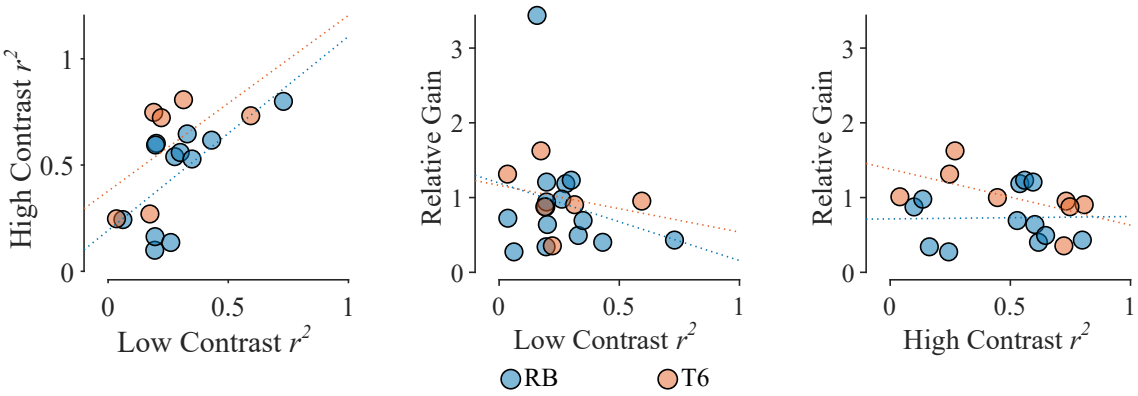


Figure 2.10: AII $E_{cat}$ model fits ($r^2$) and relative gain

These figures show the relationship between L-N model fits for each contrast condition ($r^2$), as well as the estimated relative gain change for inhibitory currents onto AII amacrine cells. As in Figure 2.9, blue points correspond to optogenetic stimulation of rod bipolar cells, while orange points indicate type-6 ON cone bipolar cells as the stimulus source. *Left* shows the positive relationship between the model fits for the two contrast conditions for both stimulus sources (suggesting that variability in model fit is a function of the individual cell recorded, *not* the contrast condition). *Center* & *right* show the poor relationship between relative gain estimate and the model fits for each contrast condition; suggesting that our gain estimates were not overly influenced by the quality of the model fits for one contrast condition of another.

when recording from ON-α cells at $E_{Cl}$ and stimulating rod bipolar cells. This shows that we can induce gain changes within the rod bipolar pathway using optogenetics ($n$ = 28, $t(27)$ = 8.88, $p<0.001$, $CI_{95\%}$ = 1.33:1.53, mean relative gain = 1.37 ±0.062).

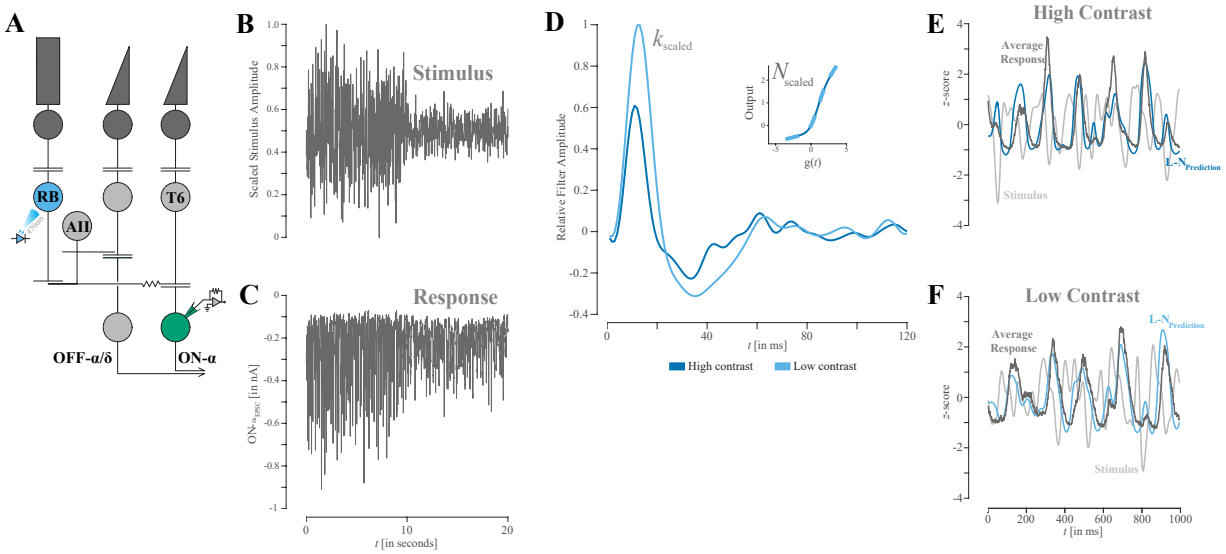


Figure 2.11: ON-α stimulated by upstream rod bipolar cells
**A**: schematic of the rod bipolar pathway, showing a rod bipolar cell (**RB**) stimulated by 470nm light (blue), and a downstream ON-α ganglion cell recorded in voltage clamp (green). **B**: an example stimulus, showing two contrast conditions (high and low), scaled to saturation and fluctuating around a mean value set to the half-max response amplitude. **C**: Corresponding excitatory post synaptic currents recorded from an ON-α ganglion cell, corresponding to the stimulus shown in **B**. **D**: the re-scaled linear kernels for the two contrast conditions, with scaled nonlinearities *insert*. The higher peak for the low contrast kernel indicates adaptation. **E**: a zoomed-in depiction of stimulus (gray), mean response (black) and L-N model fit (dark blue) for a high contrast repeat segment (note that the vertical axis is $z$-transformed for easier visualization). **F**: as **E**, but for low contrast (with L-N model fit shown in light blue).

Interestingly, while adaptation was observed in the excitatory outputs of the rod bipolar pathway when driving the circuit with ChR2-expressing rod bipolar cells, no adaptation was observed when recording the inhibitory outputs of the same stimulation source ($n$ = 13, $t(12)$ =

1.81, $p = 0.095$, $CI_{95\%} = 0.99{:}1.10$, mean relative gain = 1.05 $\pm$0.025).

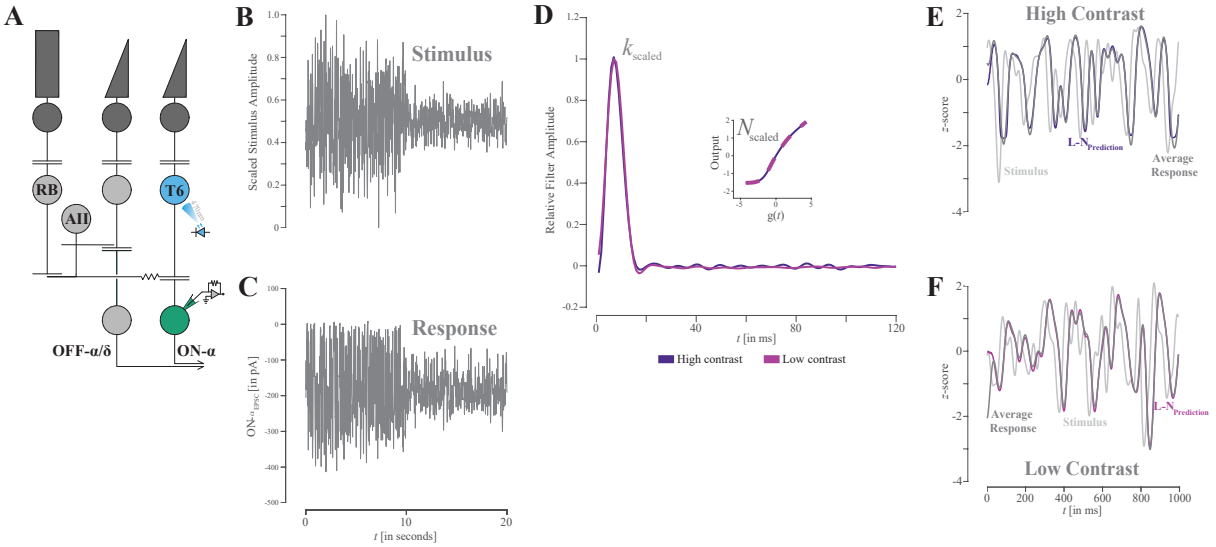


Figure 2.12: ON-α stimulated by presynaptic type-6 ON cone bipolar cells
**A**: schematic of the rod bipolar pathway, showing a type-6 ON cone bipolar cell (**T6**) stimulated by 470nm light (blue), and a downstream ON-α ganglion cell recorded in voltage clamp (green). **B**: an example stimulus, showing two contrast conditions (high and low), scaled to saturation and fluctuating around a mean value set to the half-max response amplitude. **C**: Corresponding excitatory post synaptic currents recorded from an ON-α ganglion cell, corresponding to the stimulus shown in **B**. **D**: the re-scaled linear kernels for the two contrast conditions, with scaled nonlinearities *insert*. Te equivalent peak amplitudes for the two re-scaled kernels indicates that no gain change occurs at this synapse. **E**: a zoomed-in depiction of stimulus (gray), mean response (black) and L-N model fit (purple) for a high contrast repeat segment (note that the vertical axis is $z$-transformed for easier visualization). **F**: as **E**, but for low contrast (with L-N model fit shown in pink).

Further, when stimulating ChR2-expressing type-6 ON cone bipolar cells, no gain change was observed in excitatory currents to ON-α cells either ($n = 15$, $t(14) = 0.71$, $p = 0.49$, $CI_{95\%} = 0.97{:}1.06$, mean relative gain = 1.01 $\pm$0.022). This indicates that the gain change observed in EPSCs to ON-α cells originates prior to the type-6 cone bipolar cell terminal. Perhaps more striking, it may suggest a significant difference in the overall behavior of the ribbon terminals of

rod bipolar cells and type-6 cone bipolar cells.

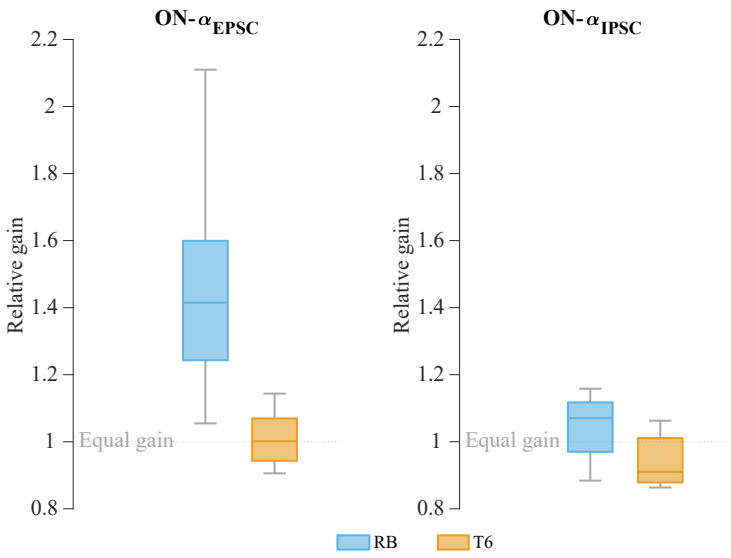


Figure 2.13: ON-α relative gain estimates by stimulus source
*Left* shows relative gain estimates for excitatory currents recorded from ON-α ganglion cells (held at $E_{Cl}$), driven by optogenetic stimulation of either rod bipolar cells (blue) or type-6 ON cone bipolar cells (orange). Note the significant gain change of signals originating from rod bipolar cells. Further, *right* shows the relative gain estimates of inhibitory currents recorded from ON-α ganglion cells (held at $E_{cat}$). No gain change was observed from either type-6 ON cone bipolar cell excitatory transmission to ON-α ganglion cells, nor for any inhibition onto ON-α ganglion cells.

Figure 2.13 shows aggregate data of the relative gain of responses driven by stimuli originating in rod bipolar cells (blue), or type-6 ON cone bipolar cells (orange). Inlaid horizontal lines demarcate no relative gain change (equivalent gain between contrast conditions, or a relative gain equal to one). The vertical axes both indicate the relative gain (assessed as the low contrast gain's peak filter amplitude normalized to the peak amplitude of the high contrast filter). *Left* shows the relative gain recorded at $E_{Cl}$, while *right* shows the relative gain recorded at $E_{cation}$. Inhibitory

currents showed no clear gain change ($n$ = 5, $t(4)$ = -2.01, $p$ = 0.115, $CI_{95\%}$ = 0.82:1.03, mean relative gain = 1.01 $\pm$0.020), while excitatory currents show a clear gain change onto ON-$\alpha$ cells when the rod bipolar pathway is driven by rod bipolar cells (as noted previously). No gain change is observed at the synapse between type-6 ON cone bipolar cells and ON-$\alpha$ ganglion cells (noted previously). Note that the increased variability in rod bipolar cell data is likely due to differences in sample size. Further, please note that a large portion of the type-6 ON cone bipolar cell data were recovered in a process described in chapter 4 of this dissertation.

Figures 2.11 & 2.12 follow the same overall layout of each example trace in this dissertation. Figure 2.11 shows that no gain change occurs at the type-6 ON cone bipolar cell to ON-$\alpha$ synapse (visible as the equal peak amplitudes of the re-scaled linear kernels in **D**). This is also demonstrated in Figure 2.13. Estimates of relative gain onto ON-$\alpha$ganglion cells for stimuli originating from type-6 ON cone bipolar cells (yellow) both sit at equal gain between contrast conditions (direct excitation, EPSCs, *left*, or indirect inhibition, IPSCs, *right*).

### 2.2.3 Synaptic depression as a source of adaptation

Figure 2.45 shows an idealized representation of readily releasable pool (RRP) dynamics within a bipolar cell, as they relate to light stimulation (adapted from Singer and Demb, 2015). In response to an initial stimulus (‘1’), vesicles are released normally. In turn, the readily releasable pool is reduced, but rapidly recovers to its baseline. With an increase in background illumination (the step shown between ‘1’ & ‘2’), the terminal treats the subsequent depolarization as an impulse of light. However, the sustained illumination after the impulse will keep the cell’s $V_m$ in a depolarized state. This leads to increased background release (*middle*). Over a short period, the

RRP more or less exhausts (*bottom*). When a subsequent pulse ('2') arrives during this elevated background illumination, the terminal has fewer vesicles to release, and each release event is lower in overall SNR (sustained release effectively being background noise here). In the case of the rod bipolar cell terminal, depletion of the RRP (ie: synaptic depression) yields synaptic adaptation to the background light level (diagram adapted from Singer and Demb, 2015).

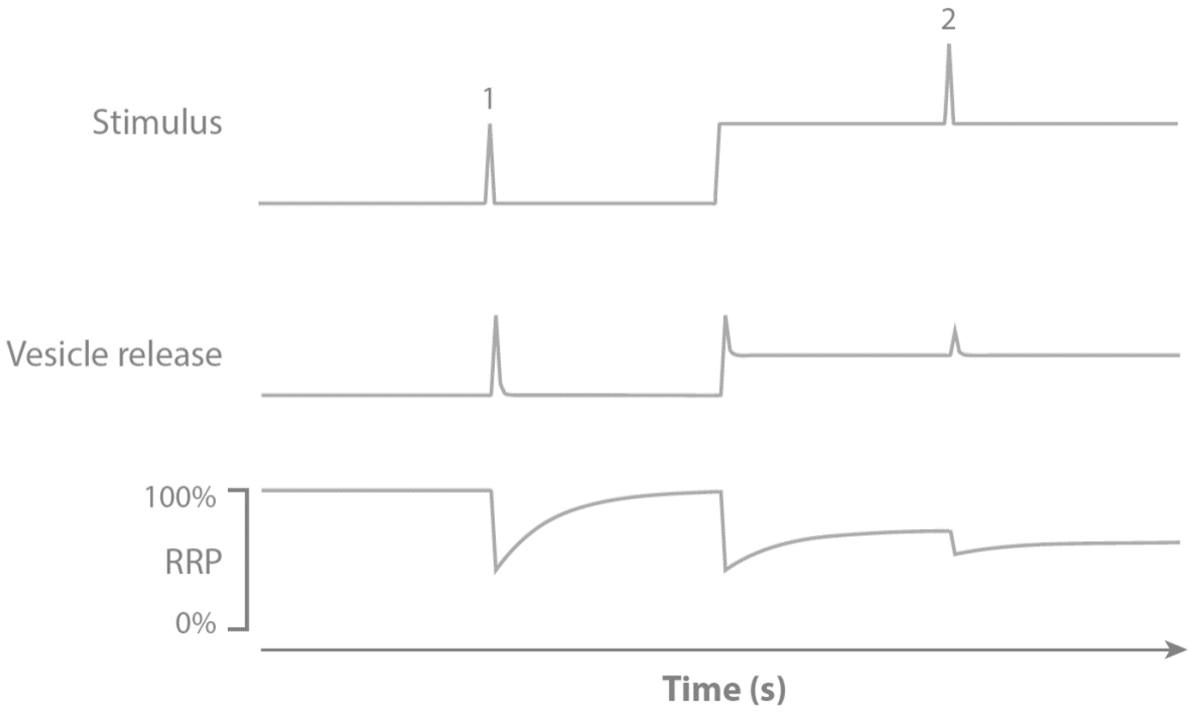


Figure 2.14: A mechanism for contrast adaptation based on readily-releasable-pool (RRP) dynamics
*Top*: light stimulus over time, *middle*: vesicle release, *bottom*: proportion of the readily releasable pool (RRP) across time. Note that sustained background illumination prevents recovery of the RRP, thereby reducing the total number of vesicles that can be released in response to further stimulation.
*Illustration adapted from Singer and Demb, 2015.*

To examine whether we could replicate synaptic depression via RRP depletion with our optogenetic model of the rod bipolar pathway, we performed a modified version of paired pulse recordings. The results of these experiments are shown in Figure 2.15. We optogenetically

stimulated rod bipolar cells and recorded EPSCs onto downstream ON-α cells (blue in **A**, **B**, & **C**). We also optogenetically stimulated type-6 ON cone bipolar cells and recorded EPSCs onto downstream ON-α cells (pink in **A**, **B**, & **C**). Finally, we recorded EPSCs from AIIs with rod bipolar cell optogenetic stimulation (green in **A**, **B**, & **C**). Note that the time points in the top plot (**B**) correspond to intended pulse intervals (horizontal axis), while the vertical axis shows the paired pulse ratio. There is a clear the difference in overall synaptic depression between rod bipolar cell terminals and type-6 ON cone bipolar cell terminals. AII recordings were more heavily impacted by an equipment issue (discussed in Chapter 4 of this dissertation) than either of the ON-α conditions. This was merely due to the order in which experiments were performed. A flaw in our equipment unfortunately led to an increased probability of dropped portions of the stimulus sequence that overlapped with the interval between pulses. As such, most of our AII paired patch recordings were discarded. To account for the possible error in timing, paired pulse data have also been plotted with binned time intervals (Figure 2.15, *bottom*, **C**). All statistical tests were run on this temporally binned paired pulse data.

Binned time points (Figure 2.15, *bottom*/**C**, horizontal axis) include any pulse interval up to and including the indicated number (but not data binned into the previous number). So, the points for $t$ = 50ms correspond to pulse intervals ranging from 10ms to 50ms, while $t$ = 100ms includes data from pulse intervals ranging from 60ms to 100ms. Finally, $t$ = 200ms was set as the upper time limit as it was roughly when pulse intervals reached an asymptote. Again, this temporal binning was necessary for most AII recordings, as well as several data points in both stimulus-source conditions of ON-α recordings. To measure the paired pulse ratio, we first took each trace and subtracted any background current from it. Then, each trace was normalized to set the peak amplitude of the first pulse to one. This was done in an effort to account for variability

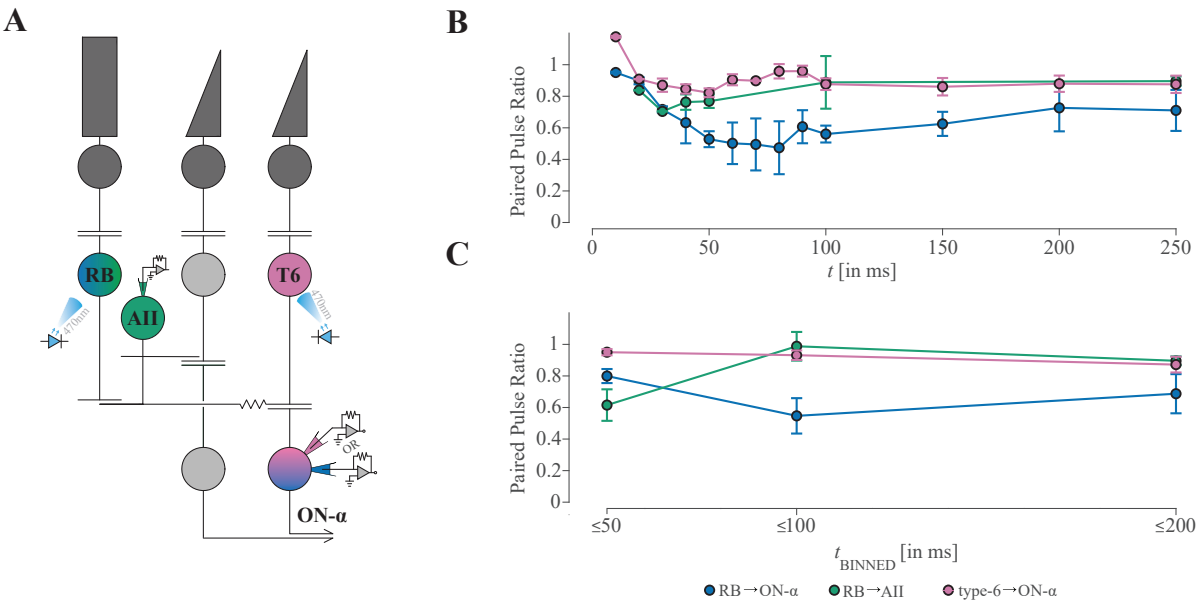


Figure 2.15: Optogenetic paired pulse results across the rod bipolar pathway

**A** shows a schematic of the rod bipolar pathway. Stimulus sources are indicated by colors corresponding to colors used in **B** & **C** (**RB**, blue/green, or **T6**, pink). Recording targets are are also indicated by colors corresponding to colors used in **B** & **C** (**ON-**α, blue/pink, or **AII**, green). Paired pulse ratios are plotted in **B** & **C**. The data shown in **B** correspond to the pulse intervals we expected when performing these experiments. The data shown in **C** are the same raw data as those in **B**, with pulse intervals binned into three intervals (horizontal axis). The reason for this temporal binning is discussed in the text, and is further explained in Chapter 4.

introduced by optogenetic rundown (discussed further in Chapter 4), as well as shifts in patch quality. Finally, the peak amplitude of the response to the second pulse was then. As the trace was already normalized, this second peak's amplitude was the paired pulse ratio (PPR). A positive PPR indicates synaptic facilitation, while a negative PPR indicates depression at the synapse.

The apparent difference in paired pulse ratio is most significant at $t_{\text{binned}}$ = 100ms. Type-6 ON cone bipolar cell terminals appear to rapidly recover from synaptic depression as compared to rod bipolar cell terminals (as seen in the overall increased PPR). Previous work has shown rapid recovery by rod bipolar cell terminals as well, though it appears that overall depression is lower (that is, the PPR is higher) for type-6 ON cone bipolar cells. Interestingly, the greatest difference is seen in rod bipolar signals recorded from ON-$\alpha$ cells. This suggests that the AII may be modulating how gain is passed onward within the circuit. ANOVA results are reported in Table 2.2.

| | ANOVA [PPR] | | | | |
|---|---|---|---|---|---|
| *Source* | *SS* | *df* | *MS* | *S.E.M.* | *p* |
| Stimulus Source [RB v. T6] | 0.42 | 2 | 0.21 | 4.35 | 0.015 |
| Pulse Interval | 0.088 | 2 | 0.044 | 0.92 | 0.40 |
| Stimulus Source * Pulse Interval | 0.48 | 4 | 0.12 | 2.49 | 0.046 |
| Error | 6.12 | 128 | 0.048 | | |
| Total | 7.12 | 136 | | | |

Table 2.2: ANOVA results for optogentic paired pulse experiments
These results show a significant difference for stimulus source on the paired pulse ratio ($p$ = 0.015). Further, an interaction between stimulus source and pulse interval was found to be significant ($p$ = 0.046), suggesting that the time course of synaptic depression is significantly different between cell types. While no significant effect of pulse interval was observed here, it is worth noting that any such effect would be obscured by the temporal binning used to analyze this data. It is likely that temporal binning also diminished the effect size observed for the interaction between stimulus source and pulse interval.

## 2.3 AII membrane potential as a modulator of adaptation

To this point, we have focused heavily on the role of synaptic processes in shaping adaptation within the rod bipolar pathway. In this section, we examine the role of the AII amacrine cell's membrane potential as a possible gain control. To examine this, we used established pharmacological methods to manipulate AII $V_m$ in conjunction with our optogenetic models (Choi et al, 2014; Cembrowski et al., 2012).

Aggregate data of the relative gain from white noise stimulation when recording excitatory currents onto ON-$\alpha$ ganglion cells can be seen in Figure 2.16. *Left* shows relative gain measurements with rod bipolar cell stimulation. Colors indicate distinct pharmacological conditions. For control ('CTRL', purple), the bath was a standard external used for all of our ChR2-related recordings (in the presence of L-AP4 and ACET). Flupirtine ('FLUP', green, 10µM) is an M-type $K^+$-channel agonist and hyperpolarizes AII amacrine cells (Adams et al., 1982a,b; Schnee and Brown, 1998; Wu et al. 2011; Choi et al., 2014). Linopirdine ('LINO', yellow, 30µM) M-type $K^+$-channel

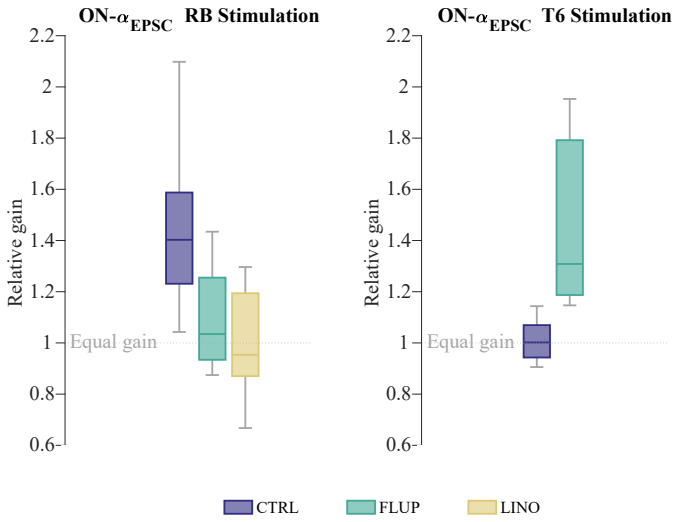


Figure 2.16: AII $V_m$ manipulation: ON pathway results

*Left* shows the relative gain change estimates for excitatory post synaptic currents recorded from ON-α ganglion cells while optogenetically stimulating rod bipolar cells. Control data are shown in purple, while green and yellow correspond to bath applied flupirtine or linopirtine respectively. *Right* shows excitatory post synaptic currents recorded from ON-α ganglion cells while optogenetically stimulating type-6 ON cone bipolar cells. Color conventions are preserved between both plots. Of note, a gain change is seen when stimulating rod bipolar cells and recording excitation onto ON-α ganglion cells, which is significantly reduces in the presence of flupirtine or linopirdine. Conversely, type-6 ON cone bipolar cell stimulation shows no change in relative gain in control conditions (as noted previously). However, bath application of flupirtine appears to cause a relative gain change that was previously absent. It is important to note that these data were heavily impacted by an issue discussed in Chapter 4, leading to the increased variability of flupirtine results, as well as the absence of linopirdine results for type-6 cell stimulation.

antagonist, and depolarizes AIIs (Cembrowski et al., 2012; Choi et al., 2014). Previous work has demonstrated that M-type currents are important in regulating the bursting behavior of AIIs, as well as spiking in other neurons (Aiken et al., 1985; Choi et al., 2014). Both flupirtine and linopirdine appeared to reduce the relative gain of signals from rod bipolar cells passing through the AII and ultimately to the ON-α. It is important to note that linopirdine seemed to significantly reduce our ability to generate L-N models, to the point of failing to produce filters. When combined with a technical issue discussed in the final chapter of this dissertation, this led to a reduced sample size and possible confounding. This may be observable in the distribution of linopirdine data, as both its skewness and kurtosis suggest inhomogeneity of variance (thereby breaking an assumption of the ANOVA). As such, a *t*-test was performed to compare the most obvious difference, a with a significant difference found for the effect of flupirtine on relative gain after both type-6 or rod bipolar stimulation via ChR2 ($T6_{stim}$: $t(14) = -4.30$, $p < 0.001$, $CI_{95\%} = -0.67{:}-0.23$, $RB_{stim}$: $t(30) = 2.46$, $p < 0.05$, $CI_{95\%} = 0.05{:}0.61$).

We also collected similar data stimulating type-6 ON cone bipolar cells and recording from postsynaptic ON-α cells at $E_{Cl}$ (Figure 2.16, *right*). Colors and axis are identical between both plots. Perhaps most interesting, flupirtine ('FLUP', green) appears to induce a gain change at the type-6 ON cone bipolar to ON-α synapse. This suggests that AII $V_m$ may be able to modulate the gain change (or lack of gain change) at the type-6 cone bipolar to ON-α synapse. By hyperpolarizing the AII network with flupirtine, we also hyperpolarized the terminals of type-6 ON cone bipolar cells. Speculatively, this could lower the probability of vesicle release. In-turn, this could make type-6 cell terminals functionally resemble rod bipolar cell terminals.

## 2.4 Discussion

In summary, we observed gain changes originating as early as the excitation from rod bipolar cells to AII amacrine cells. We did not find a gain change in inhibition evoked by rod bipolar cell stimulation onto any ON component of the rod bipolar pathway (that is, neither the AII amacrine, nor ON-$\alpha$ ganglion cell). Further, we found no gain change evoked by type-6 ON cone bipolar cell stimulation within the ON component of the rod bipolar pathway (for either excitation, or inhibition). In conjunction with previous findings (ie: Jarsky et al., 2011; Ke et al., 2014), these L-N model results confirm that the rod bipolar terminal and its synapse with the AII amacrine cell is a major contributor to adaptation within the rod bipolar pathway. Further, these data also show that type-6 ON cone bipolar cells seem to function more as a feed-forward relay of upstream gain changes (as no gain change is ever observed when signals originate with them). This rather clearly implicates a difference in how these two bipolar cell types process information.

Paired-pulse results suggest the observed difference in gain may come from a decrease in overall synaptic depression at type-6 cell terminals as compared to rod bipolar cell terminals. The only gain changes observed either excluded the type-6 cell terminal, or originated prior to it within the circuit. Speculatively, there is likely some difference in how vesicles are released at the two synapses, possibly with a far greater reserve of vesicles at the type-6 terminal (as compared to the rod bipolar terminal). This leaves the type-6 terminal ripe for future study.

Results from pharmacological manipulations of AII membrane potential also suggest that AII $V_m$ may be at the center of controlling how gain changes are propagated through the ON component of the rod bipolar pathway. It has been shown elsewhere that AIIs transmit both

sustained and transient signals through their electrical coupling with type-6 ON cone bipolar cells (Graydon et al., 2018). Determining whether the observed gain change for type-6 ON cone bipolar stimulation after application of flupirtine is at least in part by directly hyperpolarizing the type-6 cell, or through another cell (such as the more recently discovered NOS-1 amacrine cell) is beyond the capacaticy of this current work (for more on the NOS-1 cell, see: Park et al., 2020). It is possible some mechanism at the type-6 terminal is inactivated when hyperpolarizing the terminal. It is therefore, unfortunate that the experiments using linopirdine (which should depolarize the terminal) were not fruitful. The findings from manipulating AII $V_m$ further suggest that AII amacrine cells may modulate how gain changes are passed through the rest of the circuit. It has been shown elsewhere that by depolarizing the AII network, the circuit enters into a state comparable to increased background illumination. This is, in effect, similar to a sustained (or background) signal. In turn, electrical coupling between AII amacrine cells has been shown to provide noise reduction across the circuit. By pharmacologically depolarizing the coupled AII network (as with linopirdine), we made the network less sensitive to inputs from rod bipolar cells. This may explain some of the reduced model fits we found in the linopirdine condition.

A caveat must also be included regarding the AII $V_m$ manipulations discussed here. Control conditions ('CTRL', purple) were over-sampled in this data set. Due to an issue discussed in the final chapter of this dissertation, the only way to perform these analysis was to compare results as if from distinctly sampled groups (that is, not as repeated measures). Using independent samples testing like this lowers the degrees of freedom (Keppel and Wickens, 2004). This increases the probability of making Type-II errors during hypothesis testing. Thus, the chance of missing or underestimating an effect in our AII $V_m$ experiments is elevated (albeit marginally).

# Chapter 3: The OFF component of the rod bipolar pathway

The experiments up to this point have focused on the ON components of the rod bipolar pathway; namely the circuit paths leading to excitation of ON-α ganglion cells (see Figure 1). This chapter focuses on experiments to determine the loci of contrast adaptation within the remaining portion of the pathway–the OFF component.

## 3.1 Overview

The rod bipolar pathway primarily influences OFF ganglion cells through to the bistratified (and narrow-field) AII amacrine cell (Figure 3.1, 'AII', red). The dense inhibitory lobules of the AII provide direct, glycinergic inhibition to both OFF cone bipolar cell terminals (such as the type-2 OFF cone bipolar cell, orange), as well as OFF-αtype ganglion cells (such as both OFF-α and OFF-δ ganglion cells, green, Tsukamoto et al., 2001; Murphy and Rieke, 2008; Manookin et al., 2008; Münch et al., 2009; Tsukamoto and Omi, 2017; Graydon et al., 2018, Beaudoin et al., 2019). This occurs in parallel to both components of the OFF pathway, while depolarization can propagate to the ON pathway. In turn, we can drive inhibition from the AII amacrine cell onto OFF-αtype ganglion cells from two different sources–the rod bipolar cell (blue) and the type-6 ON cone bipolar cell (pink).

To further examine the mechanisms of contrast adaptation, we repeated many of the previous

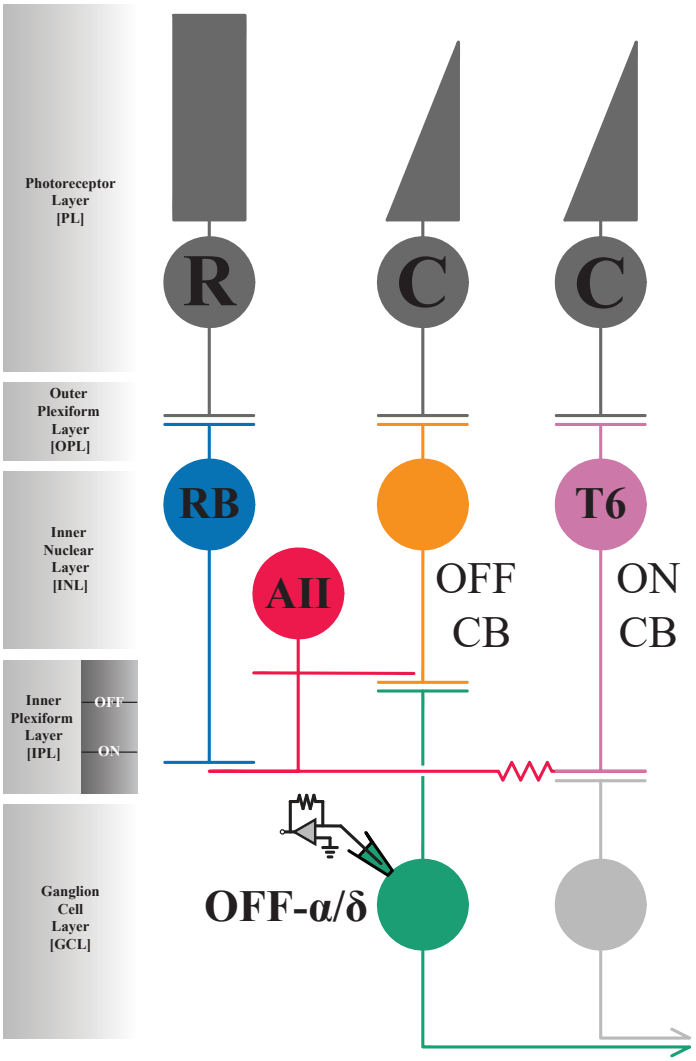


Figure 3.1: OFF component of the rod bipolar pathway

This illustration is adapted from Figure 1.1 in this dissertation, in order to highlight the paths by which signals reach OFF-α /δ ganglion cells. Rod bipolar (**RB**) signals are transmitted through excitation onto the neurites of AII amacrine cells (**AII**, red). From there, the signal propagates back, to the OFF sublaminae of the IPL. In the IPL, AIIs provide direct, glycinergic inhibition of OFF cone bipolar cell terminals (OFF CB, orange), or the dendrites of OFF-α /δ ganglion cells (**OFF-α /δ** , green). Conversely, signals from type-6 ON cone bipolar cells also use the AII to reach OFF-α /δ ganglion cells. Type-6 cells are electrically coupled to AII amacrine cells, as discussed in Chapter 1. Data presented throughout this chapter were collected by recording from OFF-αtype ganglion cells (green), and stimulating either rod bipolar cells (blue) or type-6 ON cone bipolar cells (pink).

experiments while recording from OFF-α-type ganglion cells.

## 3.2 Methods

It is important to note that most of these OFF-ganglion cells were recorded while trying to patch onto ON-α ganglion cells. As such, L-AP4 and ACET were already present in the bath solution. This precluded using normal photostimulation to reliably identify cell types (based off their transient or sustained responses to phtoostimulation). In turn, OFF-α (sustained) and OFF-δ (transient) ganglion cells have been clustered together in this data. It may be possible to parse out differences adaptation upstream of the two OFF-α-subtypes, but it would require additional experiments. Further, all methods used for recording OFF ganglion cells matched those discussed in Chapter 1. Recordings were collected exclusively at cation reversal ($E_{cat}$), in order to record inhibition onto OFF-αtype ganglion cells via the AII amacrine cell.

## 3.3 Results

Recordings were collected from OFF-α/δ retinal ganglion cells held at $E_{cat}$ (thereby recording inhibition onto those cells). Figure 3.2 shows estimations of relative gain in aggregate, while Figure 3.3 shows and L-N model fits ($r^2$) between contrast conditions. The relative gain estimates (Figure 3.2) show a gain change for both rod bipolar (blue) and type-6 ON cone-bipolar (pink) stimulation ($T6_{IPSC}$: $t(7) = 2.67$, $p<0.05$, $CI_{95\%} = 1.03{:}1.47$, $RB_{IPSC}$: $t(9) = 13.20$, $p<0.001$, $CI_{95\%} = 1.60{:}1.85$, with a significant difference between the two stimulus sources: $t(16) = -4.62$, $p<0.001$, $CI_{95\%} = -0.70{:}-0.26$). For the high contrast condition (Figure 3.3, *left*), both stimulus sources appeared to have similar model fits. However, for the low contrast condition (Figure 3.3,

*right*), a decrease in model fits for type-6 stimulation is apparent. This result was also statistically significant ($n$ = 18, $t(16)$ = -2.46, $p<0.05$, $CI_{95\%}$ = -0.53:-0.04).

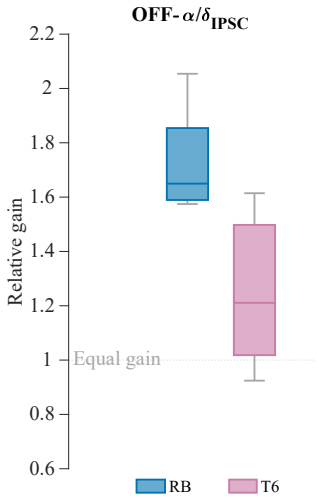


Figure 3.2: OFF-α/δ relative gain estimates
Inhibitory postsynaptic currents recorded from OFFαtype ganglion cells show a gain change for both stimulus sources (rod bipolar cells: blue, type-6 ON cone bipolar cells: pink). Further, an apparent increase in relative gain is seen when stimulating rod bipolar cells as compared to type-6 ON cone bipolar cells.

Figure 3.4 shows the aggregate model fits and relative gain as a function of contrast condition and stimulus source. The positive relationship between contrast condition $r^2$ values for L-N fit for both type-6 (orange) and rod bipolar (blue) stimulation suggests that the slight difference noted previously may not be real. However, note that the rod bipolar driven responses show a faint clustering. While not significant (RB L-N fit: $r^2$ = 0.62, $p$ = 0.57), the limitations of this work would make such an effect challenging to isolate.

Figures 22 & 23 show examples of inhibitory currents onto OFF-αtype ganglion cells,

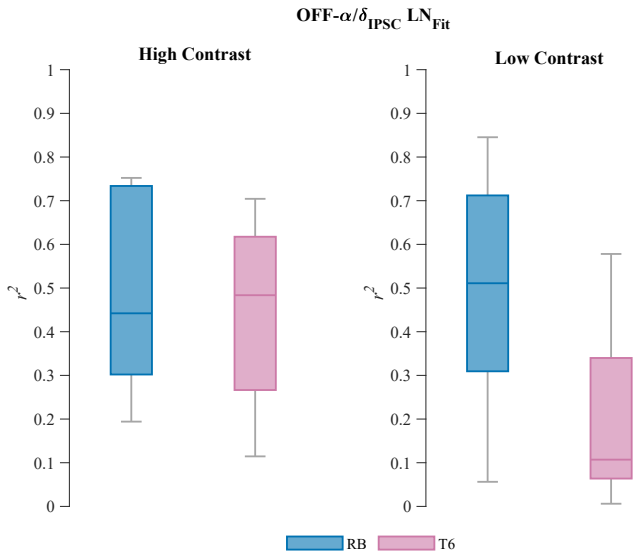


Figure 3.3: OFF-α/δ L-N model fits as a function of stimulus source and contrast condition
A comparison of L-N model fits ($r^2$ values) for inhibitory currents onto OFF-αtype ganglion cells for both rod bipolar cell (blue) and type-6 ON cone bipolar cell (pink) stimulus sources.

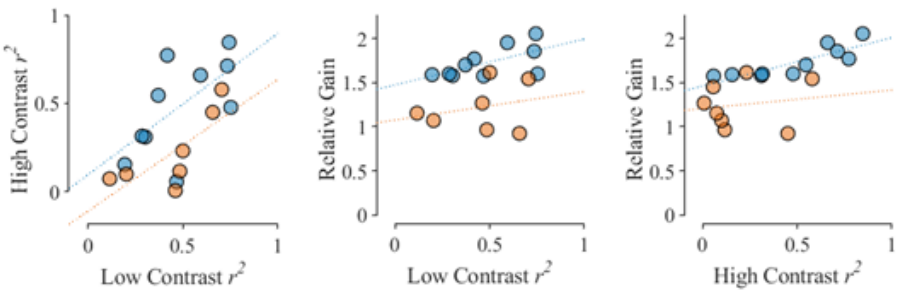


Figure 3.4: OFF-α/δ L-N model fits ($r^2$) and relative gain estimates
These figures show the relationship between L-N model fits for each contrast condition ($r^2$), as well as the estimated relative gain change for inhibitory currents onto OFF-αtype ganglion cells. As in Figure 2.9 and 2.10, blue points correspond to optogenetic stimulation of rod bipolar cells, while orange points indicate type-6 ON cone bipolar cells as the stimulus source. *Left* shows the positive relationship between the model fits for the two contrast conditions for both stimulus sources, suggesting that variability in model fit is a function of the individual cell recorded, *not* the contrast condition. *Center* & *right* show the poor relationship between relative gain estimate and the model fits for each contrast condition; suggesting that our gain estimates were not overly influenced by the quality of the model fits for one contrast condition of another. Speculatively, the faint clustering that can be observed in these figures *may* be due to differences in the inhibitory synapses from AIIs onto OFF-α versus OFF-δ ganglion cells.

during either rod bipolar cell (Figure 24, blue) or type-6 ON cone bipolar cell (Figure 25, purple) white noise stimulation. Note that both cases show a significant gain change ($RB_{stim}$: $t(9) = 13.20$, $p<0.001$, $CI_{95\%}$ = 1.60:1.85, $T6_{stim}$: $t(7) = 2.67$, $p<0.05$, $CI_{95\%}$ = 1.03:1.47), though rod-bipolar stimulation seems to evoke a larger gain change ($RB_{stim}$ gain increase: ∼72%±5.5%, $T6_{stim}$ gain increase: ∼27%±10%).

## 3.4 Discussion

These results are in agreement with our interpretations of the ON pathway data. Namely, they are consistent with adaptation occurring at the rod bipolar cell terminal, as well as within the AII network itself. As in the previous chapter (Chapter 2), it is not possible to fully rule out additional sources of gain control onto the AII amacrine cells (such as from NOS-1 amacrine cells). To examine the role of an additional amacrine cell (such as the NOS-1 cell), one might

attempt recordings from OFF-α-type ganglion cells in the presence of DNQX. This would blocking excitatory transmission and reduce the activity of any additional amacrine cells. Further, TTX may be used in the case of spiking amacrine cells, but this would hyperpolarize AII amacrine cells, and introduce a possible confound.

It is possible, that AIIs pass rod bipolar cell signals differently to the subtypes of OFF-αtype ganglion cells. Recent work has shown that AIIs break convention and also provide inhibitory synapses in otherwise ON sublaminae of the inner plexiform layer (Grimes et al., 2021). These unconventional synapses are exclusively onto OFF-α ganglion cells and not OFF-δ cells (Grimes et al., 2021). The relative proximity of this synapse to the soma of OFF-α cells could afford a better transmission of inhibitory signals from the AII for OFF-α cells versus OFF-δ cells (at least when originating as excitation from rod bipolar cells). This is outside the ability of the present data set to fully examine, but it does suggest an interesting direction for future inquiry. Namely, if this work were repeated with an initial photostimulation protocol to identify OFF-α and OFF-δ ganglion cells (in the absence of L-AP4 and ACET), one could then compare relative gain and L-N model fits between the two OFF-α ganglion cell subtypes.

Speculatively, if there is a reduction in model fit for low contrast specifically from type-6 stimulation, it may be due to the lowpass filtering of the electrical synapse between AIIs and type-6 ON cone bipolar cells, rather than some property of the AII. Additional work would be required to parse this out. Unfortunately, model fits for AIIs with type-6 ON cone bipolar cell stimulation were inconsistent, particularly for low contrast conditions (note the increased ranges for L-N model fit $r^2$ values in the low contrast condition seen in Figure 3.3, *left)*. This may have been in part due to the issues discussed in the final chapter of this dissertation, particualrly compounded by the reduced SNR in the low contrast condition. Additionally, as the low contrast

condition has lower SNR, the impact of unclamped action currents from coupled AIIs would also disproportionately influence these data. If future work demonstrates substantially better model fits for AII-inhibition onto OFF-α-type ganglion cells, then the difference in relative gain seen between stimulus sources (as in Figure 3.2) would suggest that the AII is playing a more active role in modulating how gain changes are passed through the rod bipolar pathway.

# Chapter 4: Pitfalls of L-N modeling and related methods with optogenetics

The final chapter of this dissertation focuses on a series of technical issues related to work discussed in Chapters 2 & 3. While these issues do no directly influence the interpretations of our results, they have made parsing out each effect far more challenging. The challenges faced here, and their solutions, are worth noting for anyone performing similar work.

## 4.1 Limitations of channelrhodopsin

There are a multitude of reasons for patch-clamp recordings to fail. Much of the motivation of combining optogenetics with patch physiology stemmed from making the process simpler. By stimulating a subset of cells optogenetically, we effectively clamp that entire population of cells. In turn, we remove the need for a second patch electrode in a paired patch. Further, it opens up the option of stimulating an entire component of the circuit that may be near-impossible to access in a paired-patch configuration.

Using channelrhodopsin does come with limitations. ChR2 has its own kinetics that are slower than one could achieve by driving a cell with injected current (Schneider et al., 2015). In the case of the rod bipolar cell and the rod bipolar cell to AII synapse, the result is a longer filter that doesn't fully capture the timing capability of the system (Jarsky et al., 2011). Further, channelrhodpsin-2 is permeable to cations other than $Na^+$. This may be the most challenging

component of using many optogenetic tools. The non-specific cation conductance can lead to a shift in pH, potentially hampering vesicle loading. The result can be seen in Figure 4.1. These data were collected when recording from an ON-$\alpha$ ganglion cell in whole mount, and stimulating upstream rod bipolar cells with ChR2 (illustrates in **A**). The full white noise sequence presented over one sweep is shown in **B**. In **C**, across the duration of a single sweep, response amplitude clearly declines. This figure follows the same layout convention as many others within this dissertation, with the response for a single sweep in **C** and its corresponding stimulus in **B**. Observe the rescaled filters in **D**, with green for low contrast and orange for high contrast—the gain change having been eliminated. **E** & **F** correspond to test sequences built from repeated noise sequences. Further, the nonlinearity (**D**, *insert*) shows substantial rectification and thresholding– possibly due to a disruption of normal vesicle loading and docking.

The simplest way to account for this is to manually remove portions of the noise sequence prior to constructing an L-N model. In this case, segment exclusion can be based on the performance of individual iterations of repeat noise sequences (effectively cross correlating a single repeat with the average of all other repeats). Like most system-identification methods that use kernel-based approaches, L-N modeling requires a substantial amount of actual data compared to simpler patch physiology paradigms. In turn, segment exclusions rapidly approach a point of diminishing returns, as the L-N model fit ($r^2$) can drop off substantially. To avoid this, cases where rundown were apparent were only maintained if the exclusion impacted just a single contrast condition segment.

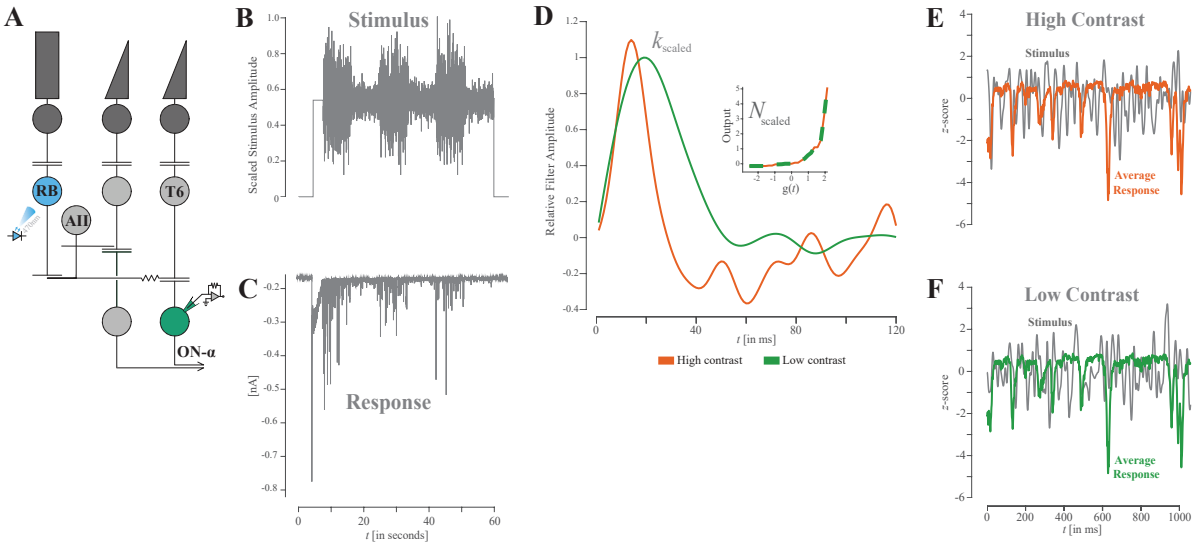


Figure 4.1: An example of optogenetic rundown

**A** shows a schematic of the rod bipolar pathway, following similar conventions to example data shown in Chapter 2 of this dissertation. In this case, a showing a ChR2-expressing rod bipolar cell (**RB**) is optogenetically stimulated with 470nm light (blue), while EPSCs are recorded from a downstream ON-α ganglion cell (green). **B** shows an example stimulus sweep, scaled to saturation and fluctuating around a mean value set to the half-max response amplitude. **C**: Corresponding EPSCs recorded from ON-α ganglion cell. Note the significant reduction in response amplitude seen across a single sweep. **D** shows the re-scaled linear kernels for the two contrast conditions, with scaled nonlinearities *insert*. Where we would normally find a gain change, we find an elimination of gain change, a slowing of the low contrast kernel, and a heavily thresholded nonlinearity. **E** & **F** show $z$-transformed stimulus (gray) and average repeat sequences (in color). Throughout the figure, orange, corresponds to high contrast while green corresponds to low contrast. Due to the substantial rundown seen in these recordings, data from this cell were excluded from analysis in prior chapters.

## 4.2 Buffer overflows

While optogenetic rundown may seem like a substantial problem, it is relatively easy to catch and account for. During the course of these experiments, I encountered a substantially more insidious problem that was extremely difficult to catch and introduced a confound that could mimic a main effect. This problem was purely hardware related. I first discovered the problem when replicating type-6 ON cone bipolar cell $V_m$ and $E_{Cl}$ recordings from CCKcreAi32 slice and found a gain change where there should not have been one. A particularly bad example of this difference in gain between conditions is shown in Figure 4.2.

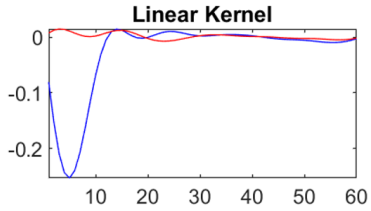


Figure 4.2: Kernel loss
Re-scaled linear kernels estimated from a type-6 ON cone bipolar cell $V_m$ recording. The blue trace is the high contrast kernel, while the red trace is the (mostly absent) low contrast kernel. Prior data suggested that these re-scaled kernels should be of equal peak amplitude and peak latency (no gain change was expected in these data).

Having confirmed the linearity of my light stimulus, the quality of my recordings, and a host of other possibilities, I traced the problem to the amplifier itself.

As it would turn out, the problem began when we switched the lab over to the Sutter d-IPA line of amplifiers. These units are an "integrated" design of patch amplifier, such that the digitizer and amplifier are all within the same device. In theory (and in most applications), this removes a serious point of failure—misalignment of the timing of acquisition between the amplifier and digitizer. In practice, the problem I uncovered stems from how the amplifier

replaces the integrated digitizer. Like a digitizer, it does have an on-board memory. However, this memory is limited, and is controlled by a USB connection (which should be substantially faster than needed for most patch recordings). Unfortunately, this makes the equipment reliant on the stability of USB-host connection between the amplifier and the computer. At one point, power fluctuations (in the form of voltage drops on the main power outlets) within the new lab space did cause host interruptions. However, a far-worse problem came from something called a buffer overflow.

It is important going into this to understand that a buffer overflow is not the root cause of aberrant behavior within the memory of a digital device. Rather, it is a symptom of something else (sometimes a fault in the physical memory, sometimes in the drivers that control it). Regardless, an example a buffer overflow is illustrated in Figure 4.3.

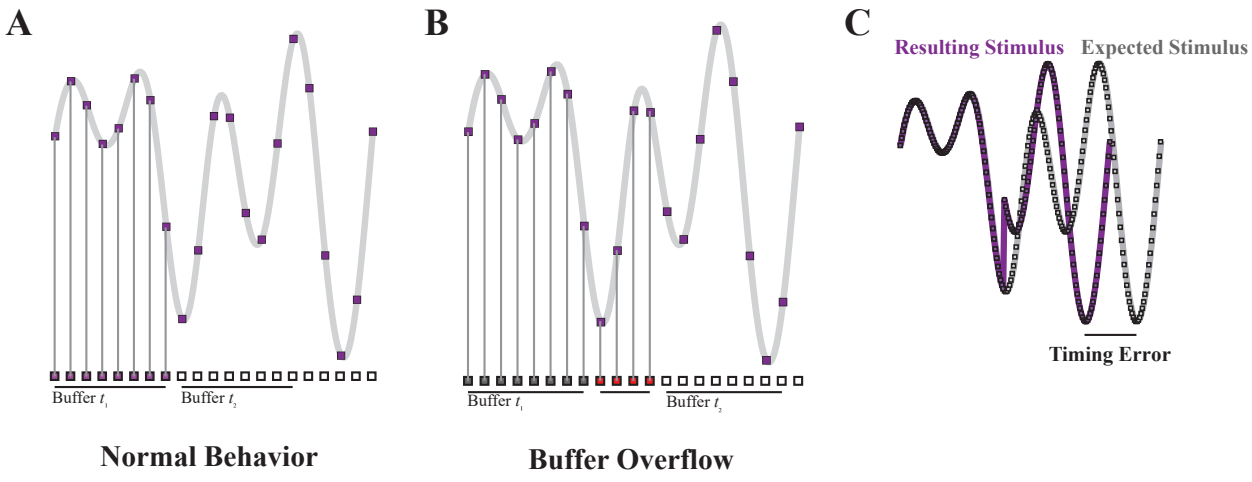


Figure 4.3: Buffer overflow illustration
**A** shows a schematic of how information should flow through a memory system during normal operation. Values from a stimulus sequence (purple points overlaying gray line) full up the buffer at a specific time point ($t_1$). **B** shows an example of how a buffer overflow can occur, where the buffer for ($t_2$) is too late to capture the four lost values (red). **C** shows an illustration of the timing error produced by lost time points due to the buffer overflow in **B**, with the expected stimulus sequence shown in gray, and the resulting stimulus shown in purple.

First, one device (or internal component of a system) sends a signal. In **A** this is illustrated as the gray noise trace. (Note: this is actually a very small portion of a noise sequence used in experiments earlier in this dissertation.) Assuming a buffer size of eight 'bits', individual points along that noise sequence are stored as numerical values in each bin of the buffer. During normal operation, the values in this buffer are used and rewritten seamlessly, with proper alignment between input and output. As the buffer empties from $t_1$, it can be filled with the next values at $t_2$. Where a problem occurs is if the timing of the two devices is out-of-sync. An example of this is illustrated in **B**, where the devices (or component) sending the signal includes four more pieces of data than the buffer has space for. In a best-case scenario, the receiving device (which contains the memory buffer) simply misses those time points in the signal, and the result is dropped frames. This results in a frame-shift/timing error between the expected and actual outputs (shown in **C**). This is, unfortunately, not the only possible outcome of a buffer overflow. The end result and behavior of the system can vary wildly depending on the design of the physical memory itself. In fact, buffer overflows are one of the more commonly exploited faults used to break the security of digital devices.

This example is also much simpler than what I actually uncovered with Sutter's IPA line of patch amplifiers. As it turns out, the buffer size and sampling rate of my data correspond to a chance of a buffer overflow roughly every four seconds for my recordings. This unfortunately (and completely coincidentally) places the first chance for a misalignment between expected and actual signal almost exactly as the white noise sequence begins (at the transition from mean background to Gaussian noise fluctuating about the mean). It also places the first chance of an overflow exactly between my first and second pulse in most of my paired-pulse data. Therefore, I elected to bin the paired pulse data shown earlier, as timing errors are nearly impossible to

account for in that data.

Finally, it is important to note that a buffer overflow in host communication (such as this) cannot be easily detected by simultaneously recording the stimulus with the same device. In fact, collecting more traces only increases the likelihood of an overflow occurring somewhere within the recording. Practically speaking, recording the stimulus sequence separately was not an option for earlier versions of this equipment, as it resulted in excessively large file sizes and limited the duration of recordings.

The first traces that confirmed the issue was at the level of the amplifier are included in Figure 4.4. Note that the traces shown are voltage signals sent by a ThorLabs light power meter via an SMA to BNC cable. The stimulus and readings were not scaled or calibrated, and the light source was not properly focused onto the light power meter. These data were merely meant to check stimulus timing. Background noise in the traces can be attributed to an impedance mismatch between the SMA and BNC connectors used by the two systems (75$\Omega$and 50$\Omega$resistances respectively), as well as poor shielding on the light meter. Later traces using a digital connection from the light meter showed lower noise levels.

The traces in Figure 4.4 show relatively good overlap for eight of ten repeats (red). The blue and green traces each show clear evidence of substantial frame drops occurring at different time points. While at a first glance the induced frameshifts appear to be integer multiples, that is not the case. In helping the team at Sutter troubleshoot and solve this problem, I collected thousands of traces like this (hoping to find a clear pattern). No clear pattern emerged other than an increased likelihood of frame drops as trials went on, and after prior frame drops (thereby compounding errors). Further, there are also smaller frame drops present within the red traces of only a few milliseconds. We accounted for some of these by lowpass filtering and downsampling our

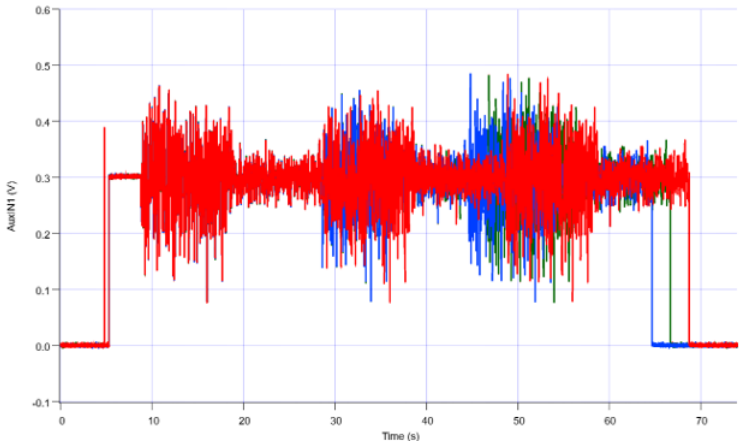


Figure 4.4: Frame drop confirmation
These traces show the time course of an identical stimulus signal output by a Sutter d-IPA amplifier. Red traces show stimulus traces in proper alignment, while the blue and green traces show misalignments that occurred during the noise presentation.

recorded data to 100Hz. While running the tests to look for a pattern in frame drop behavior, I also ran a series of test sweeps on a model cell connected through the headstage (with known stimulus pattern). Thankfully, data from the headstage were not impacted by these buffer overflows.

Prior to contacting the engineering team at Sutter Instrument Company, I asked a colleague at another institution to replicate the problem. This was in an attempt to rule out power fluctuations within the building as the root cause (an issue we had encountered previously). I asked Dr. Ruilong Hu (formerly a student in the NACS program, then a postdoctoral fellow in the Stevens Lab at The Broad Institute, now at BioMarin Pharmaceuticals) to connect a BNC cable across the 'AuxOUT' and 'AuxIN' ports and run a program that I wrote to replicate these frame drops. He did this on a Sutter IPA device (a similar model to the dIPA devices we use in the Singer Lab, with only one headstage). Other than knowing I was troubleshooting, Dr. Hu was kept blind during these recordings. Ten repetitions of the noise stimulus are shown in Figure 4.5. Note the misalignment in multiple of the traces. Further, note that this was collected using the amplifier's

data acquisition system. As such, it is possible that frame drops may have occurred in generating or recording the signal.

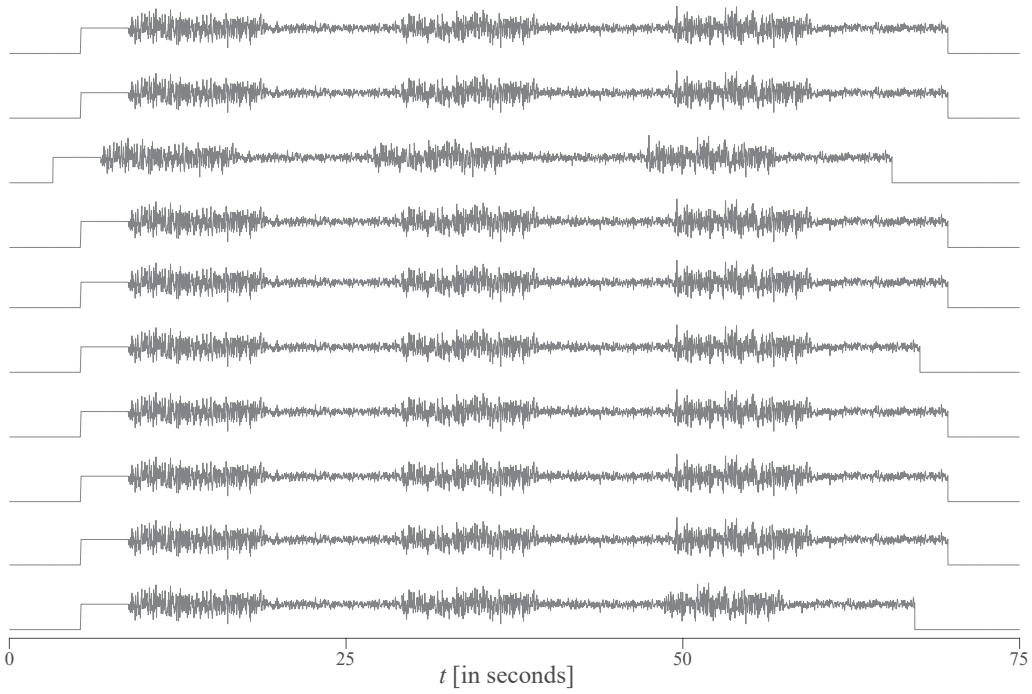


Figure 4.5: Frame drop replications collected at The Broad Institute
The data depicted above are from recording the raw output sequence from a Sutter IPA located at The Broad Institute. Along the left side of the figure, notice that the third trace starts earlier than expected. Looking along the right side of the figure, frame drops can be obeserved in several of the traces. *These data were collected by Dr. Ruilong Hu, PhD.*

While Dr. Hu was collecting that data, I also moved an amplifier and stimulus system to our previous lab space (now occupied by Dr. Speer's group), to further rule out power fluctuations. Frame drops were present in the Speer Lab space when using a Sutter d-IPA, but absent when using a MultiClamp 700B amplifier.

This problem has since been rectified by a software update for the SutterPatch acquisition software. However, the underlying cause of the buffer overflow is still unknown. To be clear, this problem was not just with my equipment. This problem impacted every single Sutter IPA unit,

regardless of operating system, age, or configuration.

## 4.3 Quantitative Methods for adjusting to incomplete L-N datasets

Solving the problem of frame drops from a buffer overflow *post hoc* was not trivial. We went through several iterations of the method. My initial idea was to use data originally collected on a MultiClamp 700B amplifier as a model to predict shifts in a cross correlogram along a rolling window (illustrated in Figure 4.6). This first pass would yield an indication of the likelihood that a frame drop had occurred. The relative positioning of that frame drop would be estimated by inverting the stimulus and response, then measuring the cross correlogram over a rolling window until a disagreement occurred. Unfortunately, this method proved infeasible as it could not be applied to all cell types or conditions.

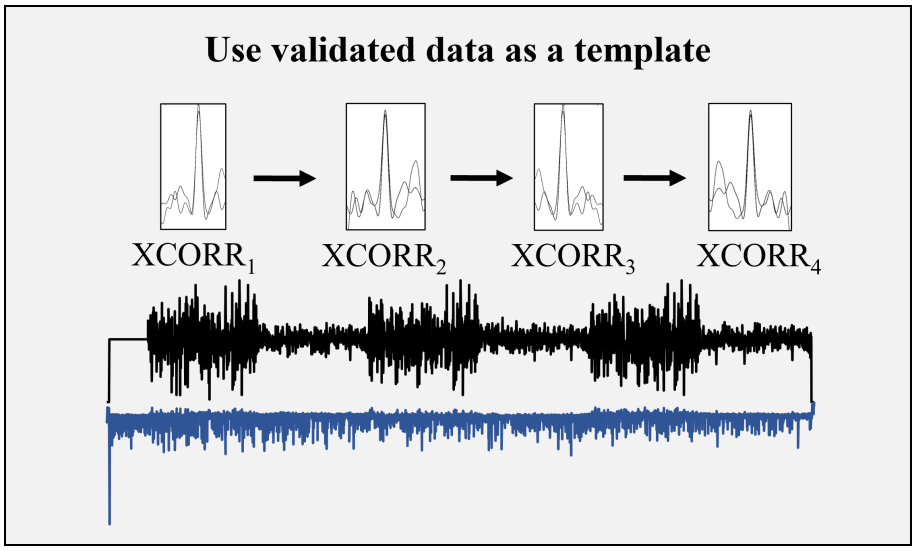


Figure 4.6: Schematic depiction of an early iteration of a frame drop detection method
The initial plan for detecting frame drops leveraged data collected on a different amplifier to estimate expected shifts in the cross correlogram ('XCORR') across a given stimulus sequence. Problems with this method are discussed in the text.

A more robust method revolved around the fact that frame drops cause a frame *shift* between the expected and actual stimulus sequences. By cross correlating the expected stimulus with actual response and including points in negative time, one can observe frame drops as a peak in negative time. An example of these can be seen in Figure 4.6 (and illustrated in Figure 4.3, **C**). This method has some limitations. Namely: multiple frame drops can occur, and it is not robust at detecting frame drops of shorter duration. Those shorter frame drops can cause a confound that mimics a gain change. The time window that can experience this confound is a function of the actual filter of the portion of the circuit being studied, which cannot be known *a priori*.

However, this method also has several advantages. First and foremost, it makes no assumption about the underlying structure of the data (other than time moving in one direction). The latency between the two peaks indicates the duration of the dropped segment (again, assuming a single drop that is long enough to reach 'negative time'). The ratio of the two peaks indicates the location of the end of the frame drop, though it is important to note that this is imperfect. By excluding segments at transition points (to maintain the assumption of orthogonality in the stimulus as part of kernel estimation), I indirectly introduce a small error into this metric (see Chapter 1, Subsection 2.3, also: Pinter and Nabet, 1992). This error compounds with the duration of the sequence (as does the probability of a frame drop occurring). That error must be accounted for during this process. Finally, by comparing the relative peak latency between contrast conditions across the 'positive' and 'negative' time peaks, this method can also indicate which contrast condition experienced a frame drop. This is also imperfect, as signal-to-noise ratio can differ substantially between contrast conditions. This also depends on the type of cell being recorded from, and type of recording being collected. An example "expanded" cross correlogram is shown in Figure 4.7, while implementation of this method is shown in Figure 4.8.

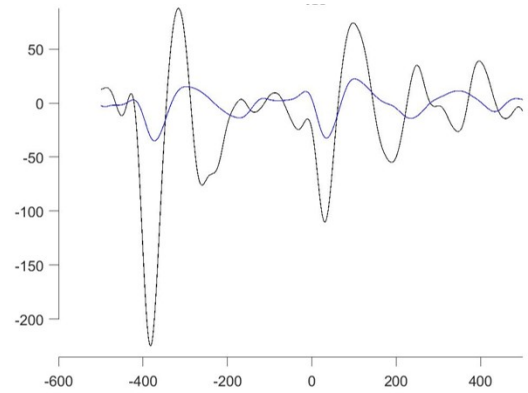


Figure 4.7: "Negative time" cross correlation
When examining a cross correlogram of the *expected* stimulus and actual response, we observed peaks in negative time. These 'negative time' peaks indicate at least one frame drop occurred. By characterizing the relationship of these two peaks, we can estimate timing, duration, and the contrast condition in which frames were dropped.

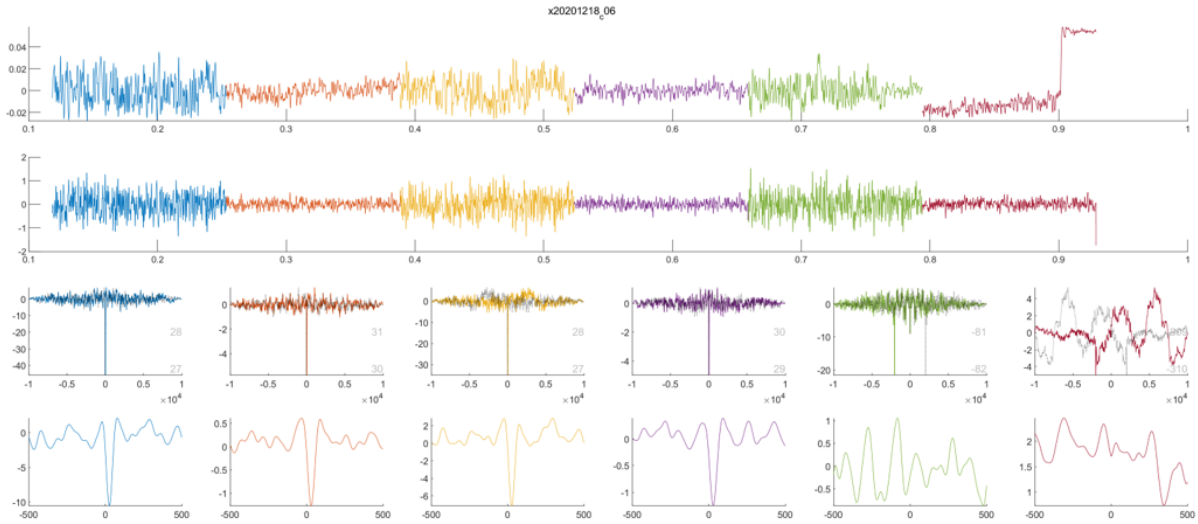


Figure 4.8: Frame drop detection implementation
Throughout this figure, colors indicate individual segments of a given contrast condition. Individual segments were analyzed to help narrow down the location of frame drops within this individual sweep. A filtered and re-scaled response sequence is shown *top*, while the corresponding *expected* stimulus sequence is shown below it. This response was a $V_m$ recording from a bipolar cell expressing ChR2. The third row of traces shows cross correlograms for the expected stimulus and actual response over entire individual contrast segments (colors indicating which segment). In these figures, the gray traces also indicate the cross correlogram measured in reverse. In the final row, we see cross correlograms for individual iterations of the repeat sequences. Observe in the red traces, a second peak emerges in the full-segment cross correlogram–indicating a frame drop.

In Figure 4.8, the *top* row indicates a recorded signal, which has been re-scaled for visualization purposes. The colors indicate different segments that were analyzed independently. The second row is the expected stimulus sequence, also mean-offset and re-scaled for visualization. Due to the type of recording shown in the top row (a current clamp recording from a type-6 ON cone bipolar cell), the frame drop may be obvious. However, it is rarely so clear when examining post synaptic currents. The third row of Figure 4.7 shows cross correlograms for the entire unique sequence within each colored segment. The fourth row shows the same for repeat sequence within each colored segment. Looking across the segments, a frame drop can be observed within the green segment. Note the dual peaks (in both positive and negative time) within the cross correlogram. Also note that each cross correlogram plot includes both forward and reverse directions. This was done to make it easier to visually detect these frame drops while manually repeating this process for every white noise trace I have *ever* collected. I also performed this frame drop detection on older data collected on an Axon Instruments MultiClamp 700B amplifier. No frame drops were detected in that data, confirming that this method has an extremely low probability of false positives.

## 4.4 Discussion

The improved 'negative time' method allowed me to recover roughly half of the data shown in this dissertation. Data were only included if frame drops impacted at most a single iteration of each contrast condition, as this was shown to have minimal impact on model performance. (Due to run-down of channelrhodopsin-2, this exclusion also increased model fit values in some cases.)

In fact, no cells were able to generate effective fits for the L-N model with any more data than that excluded. When a frame drop was detected within a segment, the entire segment was then excluded from analysis. In cases where a drop occurred prior to the final segment (Figure 4.8, red), the final segment-iteration of the opposing contrast condition was also excluded (to maintain counterbalancing). Unfortunately, a substantial amount of data were still lost to frame drops (roughly twice the data that is included here). Additional data recovery may be possible using the methods outlined above to realign stimulus and response, but this could further compound the timing errors already present. As such, it was not attempted here.

# Bibliography


Adams PR, Brown DA, Constanti A. M-currents and other potassium currents in bullfrog sympathetic neurones. *J Physiol*. 1982 Sep; 330: 537-572.

Adams PR, Brown DA, Constanti A. Pharmacological inhibition of the M-current *J Physiol*. 1982 Nov; 332: 223-262.

Aiken SP, Lampe BJ, Murphy PA, Brown BS. Reduction of spike frequency adaptation and blockade of M-current in rat CA1 pyramidal neurones by linopirdine (DuP 996), a neurotransmitter release enhancer. *Br J Pharmacol*. 1995 Aug; 115: 1163-1168.

Asari H, Meister M. Divergence of visual channels in the inner retina. *Nat Neurosci*. 2012 Nov; 15(11): 1581-1589.

Baccus SA, Meister M. Fast and slow contrast adaptation in retinal circuitry. *Neuron*. 2002 Dec 5; 36(5): 909-919.

Baden T, Berens P, Bethge M, Euler T. Spikes in Mammalian Bipolar Cells Support Temporal Layering of the Inner Retina. *Current Biology*. 2013 Dec 12; 23(1): 48–52.

Baden T, Euler T, Berens P. Understanding the retinal basis of vision across species. *Nat Rev Neurosci*. 2014 Jan; 21(1): 5-20.

Baden T, Osorio D. The Retinal Basis of Vertebrate Color Vision. *Annu Rev Vis Sci*. 2019 Sep 15; 5: 177-200.

Baylor D. How photons start vision. *Proc Natl Acad Sci*. 1996 Jan 23; 93(2): 560-565.

Baylor DA, Lamb TD, Yau KW. Responses of retinal rods to single photons. *J Physiol*. 1979 Mar; 288: 613-634.

Baylor DA, Nunn BJ, Schnapf JL. The photocurrent, noise and spectral sensitivity of rods of the monkey *Macaca fascicularis*. *J Physiol*. 1984 Dec; 357: 575-607.

Beaudoin DL, Kupershtok M, Demb JB. Selective synaptic connections in the retinal pathway for night vision. *J Comp Neurol*. 2019 Jan 1; 527(1): 117-132.

Beaudoin DL, Manookin MB, Demb JB. Distinct expressions of contrast gain control in parallel synaptic pathways converging on a retinal ganglion cell. *J Physiol*. 2008 Nov 15; 586(22): 5487-5502.

Bloomfield SA, Volgyi B. Function and plasticity of homologous coupling between AII amacrine cells. *Vision Res*. 2004 Dec; 44(28): 3297-3306.

Bloomfield SA, Xin D, Osborne T. Light-induced modulation of coupling between AII amacrine cells in the rabbit retina. *Vis Neurosci*. 1997 May-Jun; 14(3): 565-576.

Borghuis BG, Looger LL, Tomita S, Demb JB. Kainate receptors mediate signaling in both transient and sustained OFF bipolar cell pathways in mouse retina. *J Neurosci*. 2014 Apr 30; 34(18): 6128-6139

Chapot CA, Behrens C, Rogerson LE, Baden T, Pop S, Berens P, Euler T, Schubert T. Local Signals in Mouse Horizontal Cell Dendrites. *Curr Biol*. 2017 Dec 4; 27(23): 3603-3615.

Chapot CA, Euler T, Schubert T. How do horizontal cells 'talk' to cone photoreceptors? Different levels of complexity at the cone-horizontal cell synapse. *J Physiol*. 2017 Aug 15; 595(16): 5495-5506.

Cembrowski MS. *Realistic Modeling of Rod Bipolar and AII Amacrine Cells: Synaptic and Intrinsic Properties of Neurons Comprising a Retinal Microcircuit*. [Doctoral dissertation], Evanston, IL: Northwestern University; 2011.

Cembrowski MS, Logan SM, Tian M, Li W, Jia L, Kath WL, Riecke H, Singer JH. The mechanisms of repetitive spike generation in an axonless retinal interneuron. *Cell Reports*. 2012 Feb 23; 1(2): 155-166

Chavez AE, Singer JH, Diamond JS. Fast neurotransmitter release triggered by Ca influx through AMPA-type glutamate receptors. *Nature*. 2006 Oct 12; 443(7112): 705-708.

Chichilnisky EJ. A simple white noise analysis of neuronal light responses. *Network*. 2001 May; 12(2): 199-213.

Choi H, Zhang L, Cembrowski MS, et al. Intrinsic bursting of AII amacrine cells underlies oscillations in the rd1 mouse retina. *J Neurophysiol*. 2014 Sep 15; 112(6): 1491-504.

Demb JB. Functional circuitry of visual adaptation in the retina. *J Physiol*. 2008 Sep 15; 586(18): 4377-4384.

Demb JB, Singer JH. Intrinsic properties and functional circuitry of the All amacrine cell. *Vis Neurosci*. 2012 Jan; 29(1): 51-60.

Demb JB, Singer JH. Functional Circuitry of the Retina. *Annu Rev Vis Sci*. 2015 Nov 24; 1: 263-289.

DeVries SH. Bipolar cells use kainate and AMPA receptors to filter visual information into separate channels. *Neuron*. 2000 Dec; 28(3): 847-856.

Diamond JS, Grimes WN. Chapter 12: Distributed Parallel Processing in Retinal Amacrine Cells. In: Cuntz, Hermann, Remme, Michiel WH, Torben-Nielsen B, eds. *The Computing Dendrite: From Structure to Function*. 1st ed. Springer US; 2014.

Dong CJ, Hare WA. Temporal modulation of scotopic visual signals by A17 amacrine cells in mammalian retina in vivo. *J Neurophysiol*. 2003 Apr; 89(4): 2159-66.

Dowling JE *The Retina: An approachable part of the brain*. 2nd ed. Belknap Press of Harvard University Press; 2012.

Dunn FA, Doan T, Sampath AP, Rieke F. Controlling the gain of rod-mediated signals in the Mammalian retina. *J Neurosci*. 2006 Apr 12; 26(15): 3959-3970.

Dunn FA, Rieke F. The impact of photoreceptor noise on retinal gain controls. *Curr Opin Neurobiol*. 2006 Aug; 16(4): 363-370.

Dunn FA, Rieke F. Single-photon absorptions evoke synaptic depression in the retina to extend the operational range of rod vision. *Neuron*. 2008 Mar 27; 57(6): 894-904.

Euler T, Haverkamp S, Schubert T, Baden T. Retinal bipolar cells: elementary building blocks of vision. *Nat Rev Neurosci*. 2014 Aug; 15(8): 507-519.

Euler T, Masland RH. Light-evoked responses of bipolar cells in a mammalian retina. *J Neurophysiol*. 2000 Apr; 83(4): 1817-1829.

Famiglietti EV, Kolb H. A bistratified amacrine cell and synaptic cirucitry in the inner plexiform layer of the retina. *Brain Res*. 1975 Feb 7; 84(2): 293-300.

Field GD, Sampath AP, Rieke F. Retinal processing near absolute threshold: from behavior to mechanism. *Annual Review of Physiology*. 2005; 67: 1-24.

Graydon CW, Lieberman EE, Rho N, Briggman KL, Singer JH, Diamond JS. Synaptic Transfer between Rod and Cone Pathways Mediated by AII Amacrine Cells in the Mouse Retina. *Curr Biol*. 2018 Sep 10; 28(17): 2739-2751.

Grimes WN, Zhang J, Graydon CW, Kachar B, Diamond JS. Retinal parallel processors: more than 100 independent microcircuits operate within a single interneuron. *Neuron*. 2010 Mar 25; 65(2): 873-885.

Grimes WN, Zhang J, Graydon CW, et al. Complex inhibitory microcircuitry regulates retinal signaling near visual threshold. *J Neurophysiol*. 2015 Jul; 114(1): 341-353.

Grimes WN, Sedlacek M, Musgrove M, et al. Dendro-somatic synaptic inputs to ganglion cells contradict receptive field and connectivity conventions in the mammalian retina. *Current Biology*. 2021; 32: 315-328

Hampson EC, Vaney DI, Weiler R. Dopaminergic modulation of gap junction permeability between amacrine cells in mammalian retina. *J Neurosci*. 1992 Dec; 12(12): 4911-4922.

Hartveit E. Reciprocal synaptic interactions between rod bipolar cells and amacrine cells in the rat retina. *J Neurophysiol*. 1999 Jun; 81(6): 2923-2936.

Helmstaedter M, Briggman KL, Turaga SC, Jain V, Seung HS, Denk W. Connectomic reconstruction of the inner plexiform layer in the mouse retina. *Nature*. 2013 Aug 8; 500(7461): 168-174.

Ichinose T, Hellmer CB. Differential signalling and glutamate receptor compositions in the OFF bipolar cell types in the mouse retina. *J Physiol*. 2016 Feb 15; 594(4): 883-894.

Jarsky T, Cembrowski M, Logan SM, Kath WL, Riecke H, Demb JB, Singer JH. A synaptic mechanism for retinal adaptation to luminance and contrast. *J Neurosci*. 2011 Jul 27; 31(30): 11003-11015.

Jarsky T, Tian M, Singer JH. Nanodomain control of exocytosis is responsible for the signaling capability of a retinal ribbon synapse. *J Neurosci*. 2010 Sep 8; 30(36): 11885-11895.

Ke J-B, Wang YV, Borghuis BG, et al. Adaptation to background light enables contrast coding at rod bipolar cell synapses. *Neuron*. 2014 Jan 22; 81(2): 388-401.

Keppel G, Wickens TD. *Design and Analysis: A Researcher's Handbook*. 4th ed. Pearson Prentice Hall; 2004.

Kolb H, Famiglietti EV. Rod and cone pathways in the inner plexiform layer of cat retina. *Science*. 1974 Oct 4; 186(4158): 47-49.

Kolb H. Outer Plexiform Layer. In: Kolb H, Fernandez E, Nelson R, eds. *Webvision*, 2005.

Lagnado L. Ribbon synapses *Curr Biol*. 2003 Aug 19; 13(16): R631.

Lee YW, Schetzen M. Measurement of the Wiener kernels of a nonlinear system by cross-correlation. *International Journal of Control*. 1965 Mar 6; 2: 237-254.

Manookin MB, Beaudoin DL, Ernst ZR, Flagel LJ, Demb JB. Disinhibition combines with excitation to extend the operating range of the OFF visual pathway in daylight. *J Neurosci*. 2008 Apr 16; 28(16): 4136-4150.

Marmarelis PZ, Marmarelis VZ. *Analysis of physiological systems: the white-noise approach*. 1st ed., Plenum Press; 1978.

Martemyanov KA, Sampath AP. The transduction cascade in retinal ON-Bipolar cells: signal processing and disease. *Annual Review of Vision Science*. 2017 Sep 15; 3: 25-51.

Menger N, Wassle H. Morphological and physiological properties of the A17 amacrine cell of the rat retina. *Vis Neurosci*. 2000 Sep-Oct; 17(5): 769-780.

Murphy GJ, Rieke F. Network variability limits stimulus-evoked spike timing precision in retinal ganglion cells. *Neuron*. 2006 Nov 9; 52(3): 511-524.

Murphy GJ, Rieke F. Signals and noise in an inhibitory interneuron diverge to control activity in nearby retinal ganglion cells. *Nat Neurosci*. 2008 Mar; 11(3): 318-326.

Münch TA, da Silveira RA, Siegert S, Viney TJ, Awatramani GB, Roska B. Approach sensitivity in the retina processed by a multifunctional neural circuit. *Nat Neurosci*. 2009 Oct; 12(10): 1308-1316.

Nelson R, Kolb H. A17: a broad-field amacrine cell in the rod system of the cat retina. *J Neurophysiol*. 1985 Sep; 54(3): 592-614.

Oltedal L, Veruki ML, Hartveit E. Passive membrane properties and electrotonic signal processing in retinal rod bipolar cells. *Journal of Physiology*. 2009 Feb 15; 587(Pt 4): 829-849.

Park SJ, Lieberman EE, Ke J-B, Rho N, Ghorbani P, Rahmani P, Jun NY, Lee HL, Kim IJ, Briggman KL, Demb JB, Singer JH. Connectomic analysis reveals an interneuron with an integral role in the retinal circuit for night vision. *Elife*. 2020 May 15; 9: e56077.

Park SJ, Pottackal J, Ke J-B, Jun NY, Rahmani P, Kim IJ, Singer JH, Demb JB. Convergence and Divergence of CRH Amacrine Cells in Mouse Retinal Circuitry. *J Neurosci*. 2018 Apr 11; 38(15): 3753-3766.

Pinter RB, Nabet B. *Nonlinear Vision: Determination of Neural Receptive Fields, Function, and Networks*. 1st ed. CRC Press; 2012.

Roska B, Werblin F. Vertical interactions across ten parallel, stacked representations in the mammalian retina. *Nature*. 2001 Mar 29; 410(6828): 583-587.

Schnee ME, Brown BS. Selectivity of linopirdine (DuP 996), a neurotransmitter release enhancer, in blocking voltage-dependent and calcium-activated potassium currents in hippocampal neurons. *J Pharmacol Exp Ther*. 1998 Aug; 286(2): 709-717.

Schneider F, Grimm C, Hegemann P. Biophysics of Channelrhodopsin. *Annu ReV Biophys*. 2015; 44: 167–186.

Shekhar K, Lapan SW, Whitney IE, Tran NM, Macosko EZ, Kowalczyk M, Adiconis X, Levin JZ, Nemesh J, Goldman M, McCarroll SA, Cepko CL, Regev A, Sanes JR. Comprehensive Classification of Retinal Bipolar Neurons by Single-Cell Transcriptomics. *Cell*. 2016 Aug 25; 166(5): 1308-1323.

Singer JH, Diamond JS. Vesicle depletion and synaptic depression at a mammalian ribbon synapse. *J Neurophysiol*. 2006 May; 95(5): 3191-3198.

Stenkamp DL. Development of the Vertebrate Eye and Retina. *Prog Mol Biol Transl Sci*. 2015; 134: 397-414.

Szikra T, Trenholm S, Drinnenberg A, et al. Rods in daylight act as relay cells for cone driven horizontal cell-mediated surround inhibition. *Nat Neurosci*. 2014 Dec; 17(12): 1728-35.

Texler EB, Li W, Mills SL, Massey SC. Coupling from AII amacrine cells to ON cone bipolar cells is bidirectional. *J Comp Neurol*. 2001 Sep 3; 437(4): 408-22.

Thoreson WB, Mangel SC. Lateral interactions in the outer retina. *Prog Retin Eye Res*. 2012 Sep; 31(5): 407-441.

Tsukamoto Y, Morigiwa K, Ueda M, Sterling P. Microcircuits for night vision in mouse retina. *J Neurosci*. 2001 Nov 1; 21(21): 8616-8623.

Tsukamoto Y, Omi N. Functional allocation of synaptic contacts in microcircuits from rods via rod bipolar to AII amacrine cells in the mouse retina. *J Comp Neurol*. 2013 Oct 15; 521(15): 3541–3555.

Tsukamoto Y, Omi N. Classification of Mouse Retinal Bipolar Cells: Type-Specific Connectivity with Special Reference to Rod-Driven AII Amacrine Pathways. *Front Neuroanat*. 2017 Oct 24; 11: 92.

Vardi N, Smith RG. The AII amacrine network: coupling can increase correlated activity. *Vision Res*. 1996 Dec; 36(23): 3743-3757.

Veruki ML, Hartveit E. AII (Rod) amacrine cells form a network of electrically coupled interneurons in the mammalian retina. *Neuron*. 2002 Mar 14; 33(6): 935-946.

Veruki ML, Hartveit E. Electrical synapses mediate signal transmission in the rod pathway of the mammalian retina. *J Neurosci*. 2002 Dec 15; 22(24): 10558-10566.

Veruki ML, Oltedal L, Hartveit E. Electrical synapses between AII amacrine cells: dynamic range and functional consequences of variation in junctional conductance. *J Neurophysiol*. 2008 Dec; 100(6): 3305-3322.

Veruki ML, Oltedal L, Hartveit E. Electrical coupling and passive membrane properties of AII amacrine cells. *J Neurophysiol*. 2010 Mar; 103(3): 1456-1466.

Victor JD. Chapter 1: Nonlinear Systems Analysis in Vision: Overview of Kernel Methods. In: Pinter RB, Nabet B, eds. *Nonlinear Vision: Determination of Neural Receptive Fields, Function, and Networks*. 1st ed., CRC Press; 2012.

Wiener N. *Extrapolation, interpolation, and smoothing of stationary time series*. 1st ed. MIT Press; 1949.

Wiener N. *Nonlinear problems in random theory*. 1st ed. MIT Press, 1958.

Wu C, Ivanova E, Cui J, Lu Q, Pan ZH. Action potential generation at an axon initial segment-like process in the axonless retinal AII amacrine cell. *J Neurosci*. 2011 Oct 12; 31(41): 14654-14659.

Zaghloul KA, Boahen K, Demb JB. Different circuits for ON and OFF retinal ganglion cells cause different contrast sensitivities. *J Neurosci*. 2003 Apr 1; 23(7): 2645-2654.

Zhang F, Wang LP, Boyden ES, Deisseroth K. Channelrhodopsin-2 and optical control of excitable cells. *Nat Methods*. 2006; 3(10): 785-792.